

# Post-collisional magmatism: Consequences of UHPM terrane exhumation and orogen collapse, N. Qaidam UHPM belt, NW China



Mengjue Wang<sup>a</sup>, Shuguang Song<sup>a,b,\*</sup>, Yaoling Niu<sup>b,c</sup>, Li Su<sup>d</sup>

<sup>a</sup> MOE Key Laboratory of Orogenic Belt and Crustal Evolution, School of Earth and Space Sciences, Peking University, Beijing 100871, China

<sup>b</sup> Department of Earth Sciences, Durham University, Durham DH1 3LE, UK

<sup>c</sup> Institute of Oceanology, Chinese Academy of Sciences, Qingdao 266071, China

<sup>d</sup> Institute of Earth Science, Chinese University of Geosciences, Beijing 100083, China

## ARTICLE INFO

### Article history:

Received 19 June 2014

Accepted 10 October 2014

Available online 22 October 2014

### Keywords:

Post-collisional magmatism

UHPM terrane

Exhumation and extensional collapse

Mantle upwelling

North Qaidam

## ABSTRACT

Exhumation of subducted slabs and extensional collapse of orogens are the main tectonic processes in ancient and modern continental collisional zones. Magmatism during these two processes may play important roles in understanding reworking and growth of the continental crust. We report here that a series of plutonic magmas, including intrusions of two-mica granite, tonalite, granodiorite, biotite monzogranite, porphyritic biotite granite and diorite, as well as contemporaneous mafic dykes, have been recognized in Dulan eclogite-bearing terrane, the North Qaidam ultra-high pressure metamorphic (UHPM) belt. The magmatism represented by these plutons is temporally ~20–30 million years (Mys) younger than the UHPM age, lasting for ~40 Mys and derived from different sources with different mechanisms. The magmatism was initiated by exhumation of UHPM terranes during which strongly-peraluminous two-mica granite and metaluminous tonalite were produced respectively by decompression melting of the exhumed UHPM upper and lower continental crust, respectively. The genesis of mafic magmatic enclave (MME)-hosting granodiorite with a clear hybrid signature and coeval biotite monzogranite reflected the upwelling of asthenospheric mantle by extension of lithosphere during the orogen collapse. It was induced by detachment of the subducted lithospheric mantle, which then brought heat and mantle material into continental crust and triggered the partial melting of the exhumed UHPM continental crust, and gave rise to mixing of crustal and mantle melts. Porphyritic biotite granite reflects a late melting event of continental crust. Diorite marked by high magnesium content represents mantle melts with slight crustal contamination, which implies that the orogen has been unrooted and collapsed completely. The post-collisional magmatism of the North Qaidam belt provides an improved understanding for the late thermal and tectonic evolution of a UHPM continental collision zone.

© 2014 Elsevier B.V. All rights reserved.

## 1. Introduction

The generation of granitic rocks in orogenic belts plays an important role in understanding the growth and reworking of continental crust (e.g. Niu et al., 2013). The causal link between magmatism and continental subduction/exhumation, mountain building and collapse, first discussed by Dewey (1988), has been particularly stressed in the studies of lithosphere geodynamics of ultra-high pressure metamorphic terranes by means of natural and experimental investigations (Auzanneau et al., 2006; Chung et al., 2005; Hermann and Spandler, 2008; Jones et al., 1992; Ledru et al., 2001; Ma et al., 1998; Miller et al., 1999; Song et al., 2014a; Turner et al., 1996, 1999; Wallis et al.,

2005; Whitney et al., 2004; Williams et al., 2001; Zhao et al., 2011; Zheng et al., 2011). As a matter of fact, each collisional orogenic belt on Earth inevitably unroots or collapses as a consequence of gravitational equilibrium and orogen extension towards the end of each Wilson cycle (e.g. Rey et al., 2001). A transitional period after the major collision of two continents exhibits a high tendency to generate magmas of various kinds (Bonin, 2004; Liégeois et al., 1998), in which the tectonic forces and styles change with mountain building and collapse, respectively. Magmatism in this period is generally attributed to tectonic events including: (1) slab breakoff (Blanckenburg and Davies, 1995), (2) large scale lithospheric delamination (Bird, 1979), and (3) convective erosion of sub-continental lithosphere (Houseman et al., 1981). Mantle- and crustal-derived magmas can both form in response to these geodynamic processes. Mantle melts are universally marked by compositional complexity, probably due to mantle flow reorganization and mantle metasomatism during continental subduction (e.g. Duggen et al., 2005; Zhao et al., 2007), or crustal contamination

\* Corresponding author at: MOE Key Laboratory of Orogenic Belt and Crustal Evolution, School of Earth and Space Sciences, Peking University, Beijing 100871, China.  
E-mail address: [sgsong@pku.edu.cn](mailto:sgsong@pku.edu.cn) (S. Song).

(e.g. Yang et al., 2007), whereas crustal anatexis could happen during and after the initiation of continental exhumation (e.g. Labrousse et al., 2011; Song et al., 2014a), leading to generation of granitoid magmas. However, the temporal relationship between magmatism and tectonic evolution, mantle–crust interaction and generation of compositionally diverse magmatism under the post-collisional setting is poorly understood and calls for more detailed research.

While it is unclearly defined, the post-collisional geodynamic setting is likely towards the end of each Wilson cycle. This tectonic stage is thought to have the following features (Liégeois, 1998): (a) it is younger than, but still genetically related to the major collision event, (b) it has large horizontal movement of plates along mega-shear zones, and (c) it is associated with various tectonic events, leading to orogen extension and abundant magmatism. In a continental collision belt, a previously subducted oceanic slab can drag down continental lithosphere before its detachment (e.g. Song et al., 2006, 2014b). Continental crust will exhume and partially melt as a result of decompression and thermal relaxation caused by positive buoyancy. As a result of intensive changes in thermal condition, some generally refractory sources, e.g. old Archean crust, could probably melt also, making studying the petrogenesis of these igneous rocks all the more difficult. Previous studies have attempted to seek the representative post-collisional magmatism, e.g. high-K calc-alkalic and strongly peraluminous magmas (Liégeois et al., 1998), or K-rich and K-feldspar porphyritic calc-alkaline granitoids (KCG) (Barbarin, 1999). However, it remains difficult to ascribe specific magma types into the whole development of post-collisional geodynamics due to varied geological settings and evolution histories of the orogens. Researches into the post-collisional evolution of orogenic belts have presented typical magma associations that are explained as relating to slab-breakoff (e.g. Atherton and Ghani, 2002; Coulon et al., 2002; Whalen et al., 2006) or lithospheric thinning (e.g. Williams et al., 2001). In both scenarios, compositionally distinctive magmas frequently occur as a result of either simultaneous or successive mantle/crustal melting. Furthermore, in ultra-high pressure metamorphic belts, crustal melting can be readily achieved by both continental subduction and exhumation/decompression processes (e.g., Song et al., 2014a).

The North Qaidam is a well-studied UHPM belt associated with continental deep subduction and subsequent exhumation and collapse (e.g. Song et al., 2014b and the references therein). The well-documented UHP metamorphic and retrograde ages (see below) provide ideal tectonic constraints for the wide-distributed, well-preserved felsic intrusions within the North Qaidam UHPM belt. In this paper, we present detailed field, petrologic and geochemical observations to show that an integrated magmatic sequence occurred during the post-collisional stage from UHPM-terrane exhumation to orogen collapse. These studies lead us to better understand the features of the magmatism and their forming process in association with the later stage of an orogenic event.

## 2. Geological setting

The North Qaidam UHPM belt is located in the northern Tibetan Plateau. Together with the Qilian block in the north and North Qilian suture zone in the further north, the Qilian–Qaidam comprehensive orogenic system reveals an integrated orogenic process from oceanic subduction to continental collision to orogenic collapse in the Paleozoic era (e.g. Gehrels et al., 2003; J. Zhang et al., 2008; Menold et al., 2009; Song et al., 2006, 2013, 2014b; Zhang et al., 2010) (Fig. 1b). Three blocks, the Alashan block in the north, the Qilian block in the middle and the Qaidam block in the south are separated by two apparently distinct, sub-parallel, paleo-subduction zones: the North Qilian oceanic-type suture zone and the North Qaidam continental-type UHP metamorphic belt. The Qilian block in the north and the Qaidam block in the south share the same Proterozoic basement and show

close affinity to the Yangtze Craton (Song et al., 2006, 2012; Wan et al., 2001, 2006).

The North Qaidam UHP metamorphic belt extends discontinuously for 400 km between the Qilian and Qaidam blocks and comprises three major terranes (Fig. 1b). It records a complete history of the evolution of a continental orogen from early seafloor subduction, to continental collision and subduction, and to the ultimate orogen collapse in the time period from the Neoproterozoic to the Paleozoic (Song et al., 2006, 2014b; Yang et al., 2002a, 2002b). Metamorphic rocks in the three UHPM terranes include eclogite, orthogneiss, paragneiss, two-types of peridotite, and minor marble. Felsic gneisses are major components and occupy ~90% of the UHPM belt. Eclogite and two-types of peridotites occur as various-sized blocks within the felsic gneisses. This UHPM belt was believed to represent continental crust subducted to depths of 100–200 km and exhumed in the period of ~460–400 Ma (Chen et al., 2009; G. Zhang et al., 2008; J. Zhang et al., 2008; Mattinson et al., 2006a,b; Mattinson et al., 2007, 2009; Song et al., 2003a,b, 2004, 2005, 2006, 2014b; Zhang et al., 2006; Zhang et al., 2009; Zhang et al., 2010).

Retrogression followed the UHP metamorphism and produced ages between 413 and 397 Ma (Song et al., 2005, 2006; Zhang et al., 2005), reflecting a post-collisional exhumation event. The 435–410 Ma adakitic rocks that have been recognized in the Dulan terrane are interpreted as results of decompression melting of former UHP eclogites by Song et al. (2014a), or as melting of thickened lower crust during continental collision (Yu et al., 2012). Devonian granitic plutons are also reported within the North Qaidam UHPM belt (C. Wu et al., 2006; Meng and Zhang, 2008; Meng et al., 2005; Wu et al., 2007, 2009).

## 3. Petrography

Six distinct lithological types of plutons are identified intruding the Dulan UHPM terrane, including two-mica granite, tonalite, granodiorite, biotite monzogranite, porphyritic biotite granite and diorite (Fig. 1c and d). The former two types of plutons occur in the east part of the terrane and compose the “Shaliuhe granitic complex”, whereas the other four types of plutons termed “Yematan granitic complex” intrude the UHPM terrane in the west.

### 3.1. Two-mica granite

The leucocratic two-mica granite is a ~5 km<sup>2</sup> pluton (Fig. 1b), lithologically homogeneous, fine- to medium-grained, weakly foliated (Fig. 2a), and is composed of plagioclase (30%), K-feldspar (30–35%), biotite (5%), muscovite (5%), quartz (15–20%) and accessory minerals including apatite, zircon and minor opaque oxides (Fig. 3a). Muscovite is subhedral and discrete, and grows frequently associated with biotite, or as inclusions in the core of some fine-grained plagioclase crystals (Fig. 3a). Plagioclase (An<sub>17–20</sub>) is mainly fine-grained, subhedral, and displays polysynthetic twinning. K-feldspar includes orthoclase and microcline. The presence of microgranular, subhedral or anhedral microcline is indicative of a low crystallization temperature. Biotite is TiO<sub>2</sub>-rich (2.89–3.35 wt.%) in compositions with molecular Al<sub>2</sub>O<sub>3</sub>/(CaO + Na<sub>2</sub>O + K<sub>2</sub>O) ratios (Alumina Saturation index (ASI)) of 1.71–1.81. In the QAP classification diagram, the CIPW-norm compositions of the two-mica granite plot in the area of syenogranite (Fig. 4a).

### 3.2. Tonalite

The tonalite pluton occurs together with the two-mica granite, but their contact is unclear on outcrops (Fig. 1b). The south boundary of the pluton shows clear intrusive contacts with wall-rock gneissic amphibolite, and no xenoliths or enclaves were found within the pluton (Fig. 2b). The tonalite pluton is fine-grained, shows poikilitic texture and composed of biotite (15%), plagioclase (55–60%), K-feldspar (5–

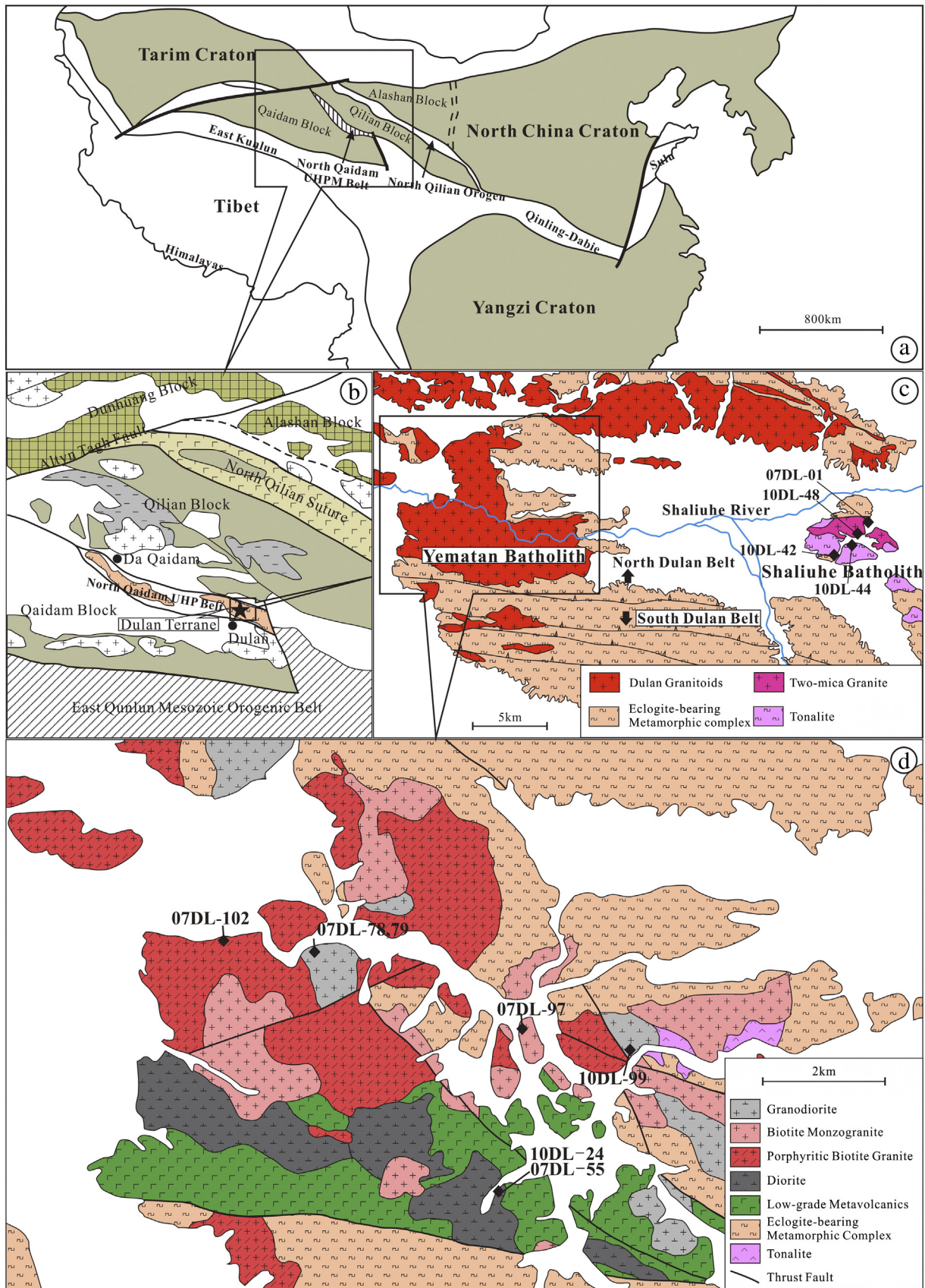


**Fig. 1.** Maps of (a) the location of Qaidam–Qilian mountain-basin system in China, (b) major tectonic units in Qaidam–Qilian mountain-basin system, (c) Dulan terrane, and (d) Yematan granitic complex. Samples were picked in the Yematan and the Shaliuhe granitic complex in the North Dulan Belt. Panel b is modified after Song et al. (2006).

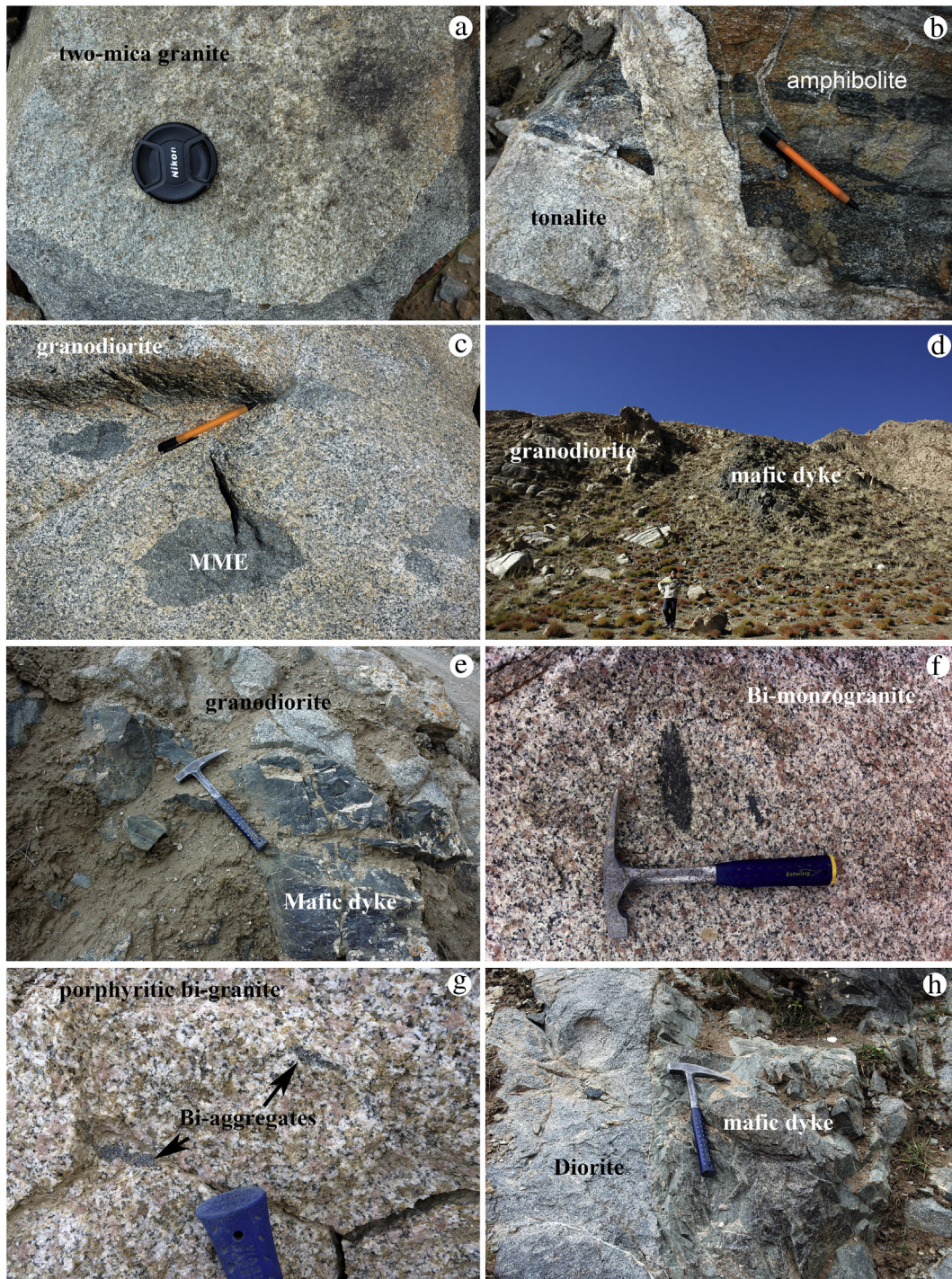


**Fig. 2.** Field photos for plutons in the Dulan UHPM terrane. (a) Two-mica granite. (b) Tonalite intruded in the metamorphic basement of the NDB. (c) Granodiorite with MMEs. (d) and (e) Mafic dykes within the granodiorite. (f) Biotite monzogranite hosting MME. (g) Porphyritic biotite granite with biotite (Bi) aggregates. (h) Diorite that intruded by mafic dyke. (For interpretation of the references to color in this figure, the reader is referred to the web version of this article.)

10%), quartz (20%), and accessories apatite, sphene, zircon and opaque oxides (Fig. 3b).

### 3.3. Granodiorite and mafic magmatic enclaves (MME)

The granodiorite crops out in the Yematan magmatic complex (Fig. 1c). It is medium- to coarse-grained, gray in color and contains a large number of mafic magmatic enclaves (MME) (Fig. 2c) and diabase dykes with clear chilled margins. The granodiorite shows poikilitic texture and consists of hornblende (10–15%), biotite (5%), plagioclase

(An<sub>32–48</sub>, 40–45%), K-feldspar (10–15%), quartz (15–20%) and accessories apatite, zircon and opaque oxides (Fig. 3c).

Mafic enclaves are ellipsoidal and slightly oriented, ranging in size from several to tens of centimeters. They show homogeneous, fine-grained texture with mineral assemblage of hornblende (40–45%), plagioclase (An<sub>27–46</sub>, 45–50%), biotite (5%) and quartz (0–5%). Ferro-magnesian minerals in enclaves increase both in abundance and grain size from the rim to the core, resembling typical mafic magmatic enclave (MME) (e.g. Hibbard, 1991). Abnormal zoning is identified within some large plagioclase crystals, which shows irregular An changing

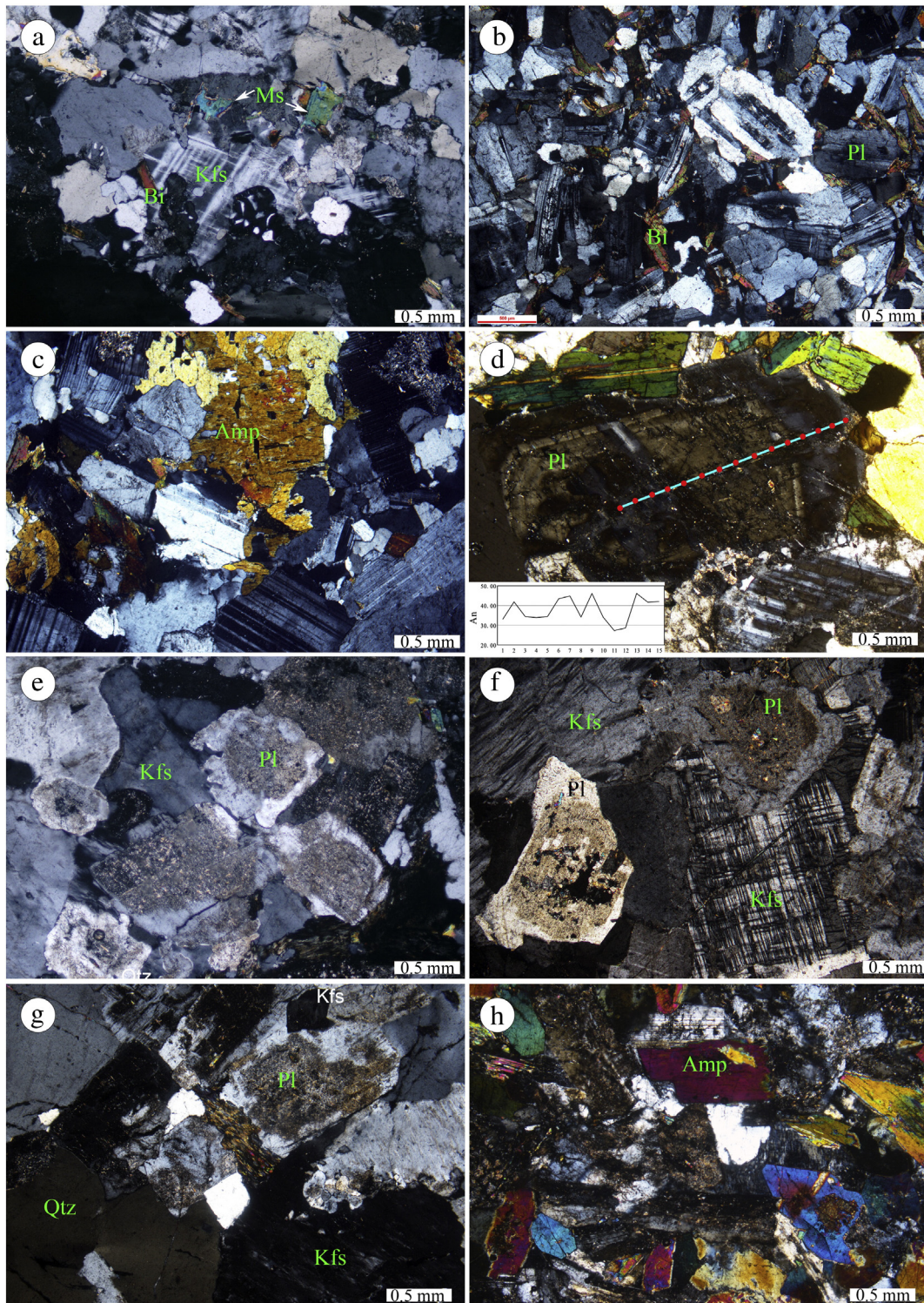


**Fig. 3.** Microscopic photos for plutons in the Dulan UHPM terrane. (a) Two-mica granite. (b) Tonalite. (c) Granodiorite. (d) Plagioclase phenocryst in the MME, with the An diagram at bottom left showing abnormal zoning. (e) Biotite monzogranite. (f) Biotite monzogranite with abundant microcline. (g) Porphyritic biotite granite. (h) Diorite.

from core to rim (Fig. 3d). Disequilibrium textures such as needle-like apatites are also observed.

#### 3.4. Biotite monzogranite

The biotite monzogranite pluton is apparently reddish in color (Fig. 2d) and closely associated with the granodiorite (Fig. 1c). It is composed of biotite (<5%), plagioclase (35–40%), K-feldspar (30–35%),

quartz (20–25%), and accessories apatite and zircon. Biotite is brown and euhedral, partly replaced by chlorite. Plagioclase is often sericitized with translucent cores surrounded by Na-rich, transparent rims of low An = 8–10% (Fig. 3e). K-feldspar, often with perthitic exsolution lamellae, occurs as anhedral grains between euhedral plagioclase crystals, and has biotite and plagioclase inclusions, reflecting its later crystallization. Microcline is locally abundant (Fig. 3f), but orthoclase is more common.

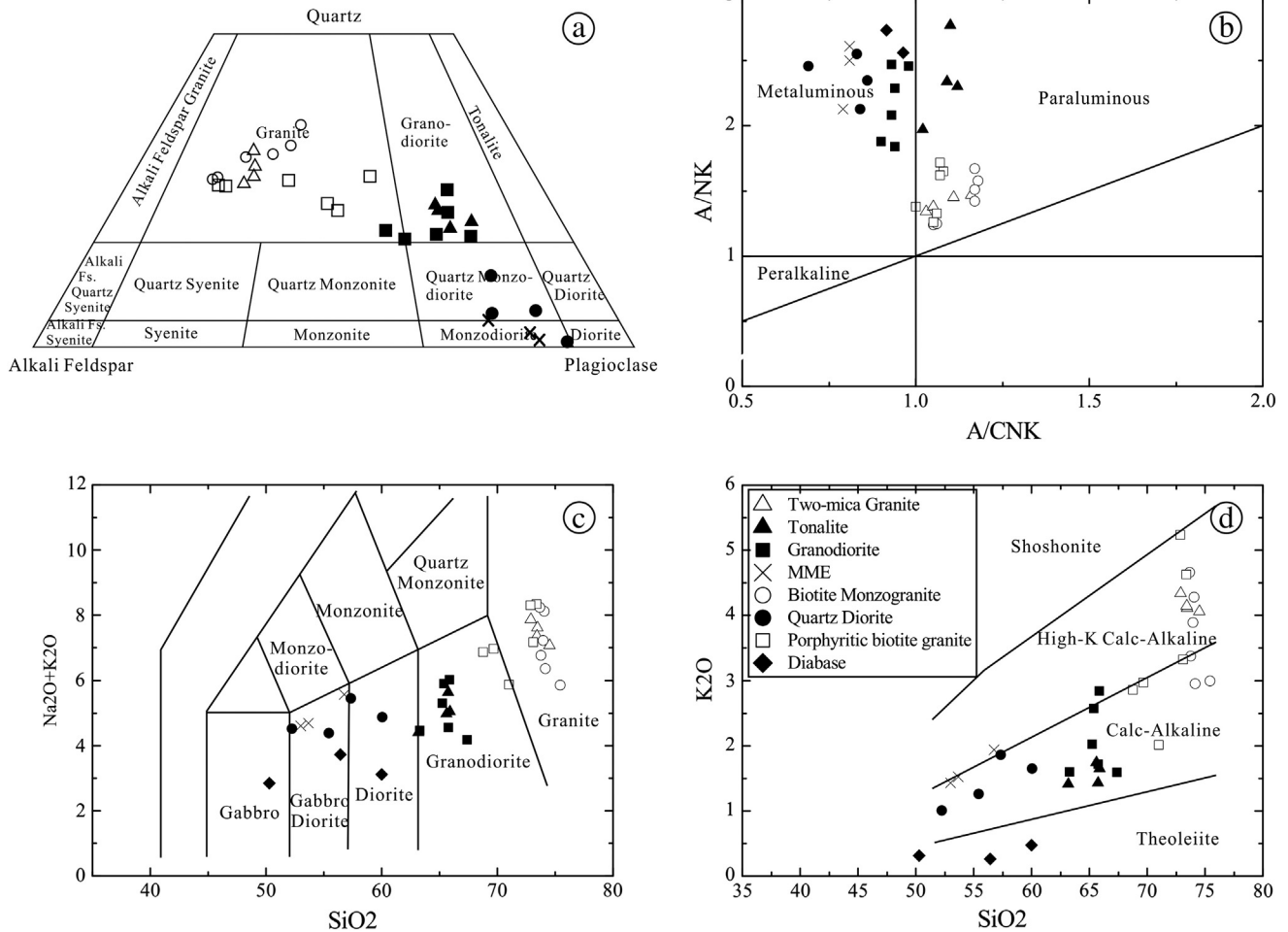


Fig. 4. (a) QAP diagram. (b) A/NK-A/CNK diagram. (c) TAS diagram. (d)  $K_2O$ - $SiO_2$  diagram for plutons in the Dulan UHPM terrane.

### 3.5. Porphyritic biotite granite

The porphyritic biotite granite crops out over 15 km<sup>2</sup> and forms the major part of the Yematan granitoid complex (Fig. 1c). It apparently shows pale-reddish in color, coarse-grained porphyritic texture with rare, irregular-shaped biotite-rich enclaves (Fig. 2e). The mineral assemblage in this rock includes plagioclase (30–35%), K-feldspar (35–40%), quartz (20–25%), minor biotite and accessories apatite and sphene. Biotite is dark brown, euhedral and blade-shaped, and mostly altered into chlorite. Plagioclase ( $An_{22-27}$ ) is a euhedral tabular crystal with altered An-rich core and clean Ab-rich rim (Fig. 3g). K-feldspar includes orthoclase and perthite, and occurs as anhedral, coarse-grained or porphyritic crystals with biotite and plagioclase inclusions.

### 3.6. Diorite

The diorite intrusion occurs as an elongate pluton of 1.5 × 8 km<sup>2</sup> in the southern part of the Yematan granitoid complex (Fig. 1c). It is composed of hornblende (30–35%), plagioclase (45–50%), quartz (0–5%), K-feldspar (5%), and accessories apatite and opaque oxides (Figs. 2h and 3h). Hornblende is tawny, euhedral and displays simple twinning and has higher Mg content [ $Mg/(Mg + Fe^{2+}) > 0.65$ ] than hornblendes in the granodiorite or enclaves. Plagioclase ( $An_{21-41}$ ) is subhedral and strongly altered. Quartz and K-feldspar (orthoclase) are both fine-grained anhedral crystals. They crystallized much later and filled in the space between plagioclase and hornblende. Fine-grained mafic dykes were also observed in the diorite pluton (Fig. 2h).

## 4. Geochemistry

### 4.1. Analytical method

Mineral analyses were conducted using a JXA-8100 electron microprobe at MOE Key Laboratory of Orogenic Belt and Crustal Evolution, Peking University. The analytical conditions were 15 kV accelerating voltage and 10 nA beam current with a beam diameter of 1 μm. The mineral standards used for calibration include the 53 minerals from SPI Co. Ltd., US. The analysis accuracy is better than 5%.

Zircon grains were separated using combined methods of magnetic and heavy-liquid separation, and then handpicked under a binocular. Representative zircon grains were set in an epoxy mount and polished to half thickness. CL images were taken at Peking University using a CL spectrometer equipped on a Quanta 200F ESEM with 2-min scanning time under 15 kV and 120 nA. Measurements of U, Th and Pb were conducted at the Geological Lab Center, China University of Geosciences, Beijing (CUGB) using an Agilent 7500a inductively coupled plasma mass spectrometry (ICP-MS) with New Wave UP 193SS laser ablation system. The spot diameter was 36 μm and the laser frequency was 10 Hz. The measured U–Pb isotopic ratios were corrected on the basis of the measurement of isotopic ratios of standard zircon 915 and TEMORA and then were used in GLITTER 4.4 to calculate the U–Pb isotope composition. Common lead correction was following the procedure in Andersen (2002). The weighted mean <sup>206</sup>Pb/<sup>238</sup>U ages were calculated using Isoplot3 (Ludwig, 2003).

Analysis of major and trace element composition was conducted at CUGB using Leeman Prodigy inductively coupled plasma-optical emission spectroscopy (ICP-OES) and an Agilent-7500a ICP-MS. The analytical details with precisions and accuracies are as given in Song et al. (2010).

Sample dissolution, the separation of Sr, REE and of Sm–Nd was conducted at MOE Key Laboratory of Orogenic Belt and Crustal Evolution, Peking University. The experimental procedure is the same as in Jahu et al. (1996). Rb–Sr and Sm–Nd isotopic compositions were determined using Triton thermal ionization mass spectrometry (TIMS) at Tianjin Institute of Geology and Mineral Resources. Measurement of JNDI Nd standard and NBS-987 Sr standard yielded  $^{143}\text{Nd}/^{144}\text{Nd} = 0.512118 \pm 6$  ( $2\sigma$ ,  $N = 5$ ) and  $^{87}\text{Sr}/^{86}\text{Sr} = 0.710238 \pm 5$  ( $2\sigma$ ,  $N = 3$ ). Measured Nd and Sr isotopes were normalized to  $^{146}\text{Nd}/^{144}\text{Nd} = 0.7219$  and  $^{86}\text{Sr}/^{88}\text{Sr} = 0.1194$ , respectively. Initial  $^{143}\text{Nd}/^{144}\text{Nd}$  and  $\varepsilon_{\text{Nd}}(t)$  were calculated based on the present-day CHUR values of  $(^{143}\text{Nd}/^{144}\text{Nd})_{\text{CHUR}} = 0.512638$  and  $(^{147}\text{Sm}/^{144}\text{Nd})_{\text{CHUR}} = 0.1967$ .

Analysis of zircon Hf isotope was carried out using a New Wave UP213 laser-ablation microprobe, attached to a Neptune multi-collector ICP-MS at MLR Key Laboratory of Metallogeny and Mineral Assessment, Institute of Mineral Resources, Chinese Academy of Geological Sciences, Beijing. Instrumental conditions and data acquisition were described by Hou et al. (2007). The laser system uses beam diameter of either 40  $\mu\text{m}$  or 55  $\mu\text{m}$  on the basis of the zircon size. Isobaric interference correction and instrumental mass bias correction of Lu, Yb and Hf isotopes are conducted as described by Chu et al. (2002), F.-Y. Wu et al. (2006) and Hou et al. (2007). Zircon GJ1 was used as the standard with a weighted mean  $^{176}\text{Hf}/^{177}\text{Hf}$  ratio of  $0.281998 \pm 0.000021$  ( $2\sigma$ ,  $n = 13$ ).

#### 4.2. Major and trace elements

Major and trace element data are listed in Appendix Table 1. Geochemical diagrams of each plutonic unit are shown and Figs. 4, 5, and 6.

#### 4.2.1. Two-mica granite

Four two-mica granite samples exhibit homogeneous compositions with high  $\text{SiO}_2$  (72.90–74.50 wt.%),  $\text{K}_2\text{O}$  (4.06–4.34 wt.%), and  $\text{K}_2\text{O}/\text{Na}_2\text{O}$  ratio (1.17–1.35), medium total alkaline ( $\text{Na}_2\text{O} + \text{K}_2\text{O} = 7.07$ –7.87 wt.%), and plot in the granite field of the TAS diagram (Fig. 4c). All the samples are peraluminous with alumina saturation index (ASI) ratios of 1.03 to 1.16 (Fig. 4b). Samples of the two-mica granite have high abundances of rare earth elements (REE) ( $\Sigma\text{REE} = 170$ –194 ppm). The chondrite-normalized REE patterns are characterized by high LREE ( $[\text{La}/\text{Sm}]_{\text{N}} = 4.7$ –5.4), relatively flat HREE ( $[\text{Gd}/\text{Yb}]_{\text{N}} = 1.9$ –2.5) and a pronounced negative Eu anomaly ( $\text{Eu}/\text{Eu}^* = 0.35$ –0.42) (Fig. 5a). The primitive-mantle normalized trace element diagram shows characteristic negative anomalies in Ba, Sr, Eu and HFSEs (Nb, Ta, Ti and P) and positive anomalies in Rb, Th, U and Pb (Fig. 6a).

#### 4.2.2. Tonalite

Four tonalite samples exhibit a narrow compositional range of  $\text{SiO}_2$  (63.19–65.89 wt.%),  $\text{Al}_2\text{O}_3$  (16.70–17.87 wt.%) and  $\text{MgO}$  (1.59–2.30 wt.%) and low  $\text{K}_2\text{O}/\text{Na}_2\text{O}$  ratios of 0.34–0.54 and ASI 1.02–1.12 (Fig. 4b and c). They have relatively low REE contents ( $\Sigma\text{REE} = 65$ –118 ppm) and show a LREE enriched ( $(\text{La}/\text{Yb})_{\text{N}} = 5.0$ –20.5) pattern with a weak negative or slightly positive Eu anomaly ( $\text{Eu}^* = 0.72$ –1.03) (Fig. 5b). Both Sr (290–400 ppm) and Sr/Y ratios (15–27) are lower than the typical adakites. In the primitive-mantle normalized trace element diagram, all samples show relatively weak Nb, Ti and P depletion and Rb enrichment (Fig. 6b).

#### 4.2.3. Granodiorite and MME

Six samples from the granodiorite pluton are plotted within the granodiorite field (Fig. 4c). They are all calc-alkaline and metaluminous ( $\text{ASI} = 0.90$ –0.98) (Fig. 4b), consistent with the I-type granitoids (Wu et al., 2000). The granodiorite samples show slightly fractionated REE

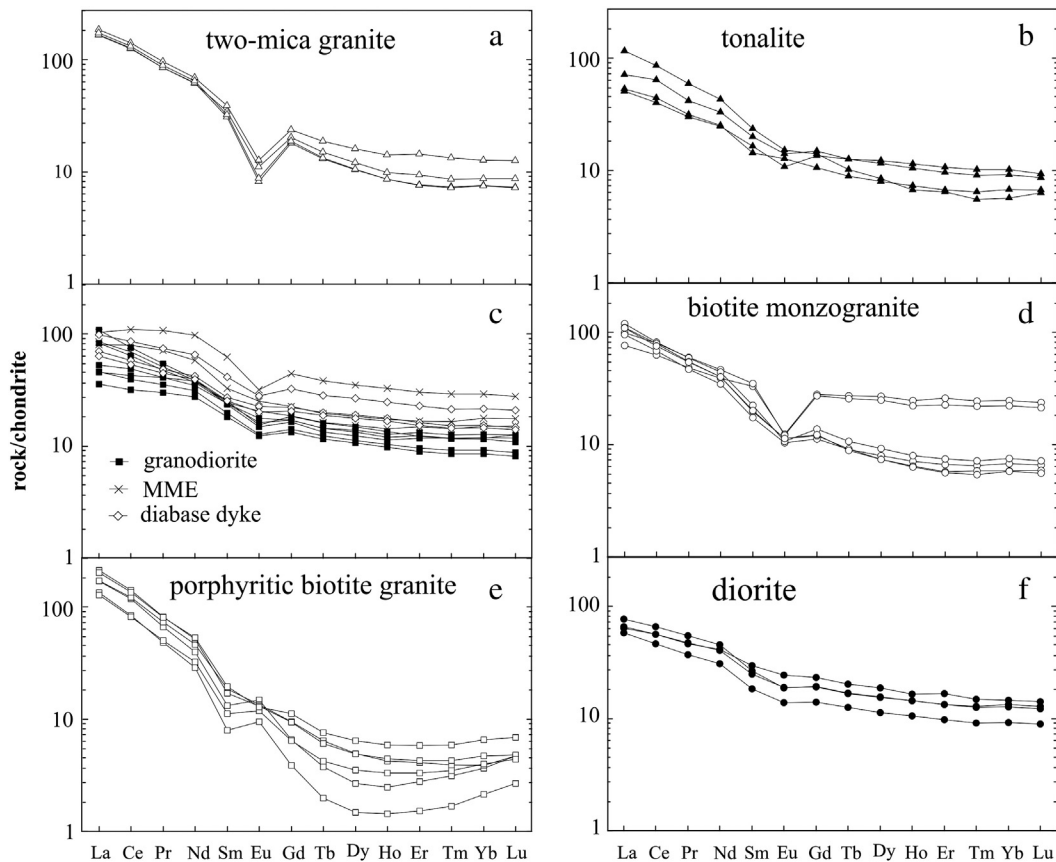


Fig. 5. Chondrite-normalized REE (Sun and McDonough, 1989) patterns for plutons in the Dulan UHPM terrane.

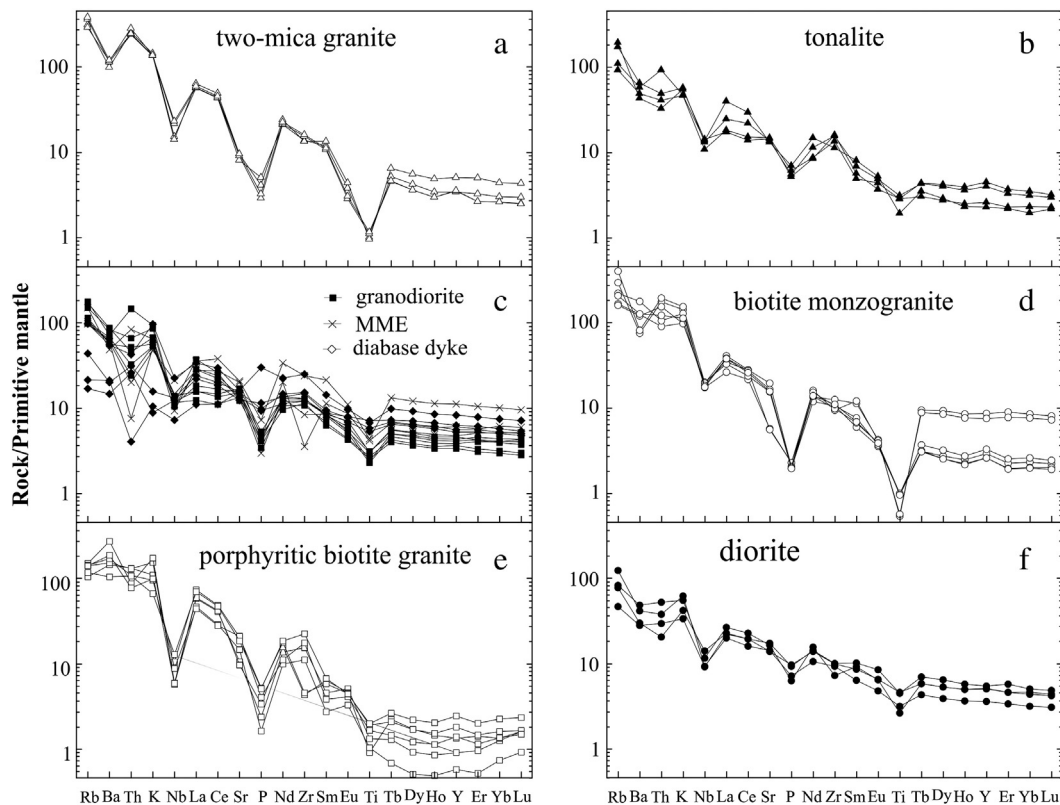


Fig. 6. Primitive mantle normalized (Sun and McDonough, 1989) trace element diagrams for plutons in the Dulan UHPM terrane.

patterns with LREE enrichment ( $(La/Yb)_N = 4.0\text{--}9.2$ ) and weak negative Eu anomaly ( $Eu^* = 0.72\text{--}0.88$ ; Fig. 5c). The primitive-mantle normalized trace element diagram exhibits distinct Ti, P depletion and LILE and Th, U, Pb enrichment (Fig. 6c).

Two MME samples are intermediate ( $SiO_2 = 53.69\text{--}56.78$  wt.%) with  $K_2O/Na_2O$  ratio of 0.45–0.54. They have higher REE concentrations ( $\Sigma REE = 105\text{--}192$  ppm) than the host granodiorite (57–112 ppm) and show weak LREE enrichment ( $(La/Yb)_n = 3.5\text{--}5.7$ ) with intermediate Eu anomaly ( $Eu^* = 0.69\text{--}0.96$ ) (Fig. 5c). The primitive-mantle normalized trace element diagrams show similar patterns to the host granodiorite (Fig. 6c).

Three diabase dyke samples are intermediate ( $SiO_2 = 50.30\text{--}60.02$  wt.%) with high MgO (5.24–6.82 wt.%) and low  $K_2O/Na_2O$  ratio of 0.05–0.18 (Fig. 4c and d). They have relatively lower REEs ( $\Sigma REE = 70\text{--}99$  ppm) and a flat REE pattern ( $(La/Yb)_n = 1.9\text{--}4.6$ ) with no Eu anomaly ( $Eu^* = 0.88\text{--}0.96$ ) (Fig. 5c).

#### 4.2.4. Biotite monzogranite

Geochemically, the six biotite monzogranite samples can be subdivided into two groups; they all exhibit high  $SiO_2$  (73.65–75.45 wt.%), and low  $TiO_2$  (0.11–0.19 wt.%), MgO (0.22–0.57 wt.%) and CaO (1.06–1.83 wt.%), but are different in  $K_2O$  (2.95–4.66 wt.%) and  $K_2O/Na_2O$  (0.86–1.30) (Fig. 4c and d). All samples plot in the peraluminous field and are weakly or strongly peraluminous ( $ASI = 1.05\text{--}1.18$ ). The two strongly peraluminous samples ( $ASI = 1.18$ ) have high HREEs with a distinct negative Eu anomaly ( $Eu^* < 0.5$ ) (Fig. 5d), while the other four samples show significant LREE enrichment ( $(La/Yb)_n = 3.1\text{--}19.1$ ) with a relatively weak Eu anomaly ( $Eu^* > 0.5$ ). Nb, Ti, and P are strongly depleted with Rb, Th, and U highly enriched (Fig. 6d).

#### 4.2.5. Porphyritic biotite granite

Six porphyritic biotite granite samples are calc- to high-K calc alkaline, and weakly peraluminous ( $A/CNK = 1.00\text{--}1.08$ ). They show

concave REE patterns with LREE enrichment ( $(La/Yb)_N = 30.90\text{--}63.18$ ) and MREE depletion (Fig. 5e) with a positive anomaly ( $Eu^* = 1.01\text{--}1.71$  except for 10DL-10). In the spidergram (Fig. 6e), all samples show obvious Nb, P and Ti depletion.

#### 4.2.6. Diorite

Four diorite and dioritic dyke samples are calc-alkaline and metaluminous (Fig. 4b) and plot in the diorite field (Fig. 4a). The mg-numbers of the diorite are constantly high [molar  $100 * Mg/(Mg + Fe^{2+}) = 64\text{--}71$ ] relative to melts from lower crust, or metasomatized lithospheric mantle (e.g., Xu et al., 2002). Chondrite-normalized REE patterns are slightly fractionated ( $(La/Yb)_n = 4.4\text{--}6.3$ ) with a weak negative Eu anomaly ( $Eu^* = 0.83\text{--}0.93$ ) (Fig. 5f). Nb, Ti and P are depleted in primitive mantle-normalized spidergram while LILEs and Th are mildly enriched (Fig. 6f).

### 4.3. Whole-rock Sr–Nd isotopes

Seventeen representative samples for all the six major types of lithologies, MME and diabase dyke were analyzed for whole-rock Sr–Nd isotopes. The data are given in Appendix Table 2 and plotted in Fig. 7. The initial  $^{87}Sr/^{86}Sr$  ( $I_{Sr}$ ) and  $\epsilon_{Nd}$  were calculated at 400 Ma.

The plutons in the Dulan UHPM terrane show strong heterogeneity in Sr and Nd isotope compositions. Two two-mica granite samples exhibit the most negative  $\epsilon_{Nd}(t)$  of  $-6.6$  to  $-7.3$  and nearly identical  $I_{Sr}$  of 0.7117 with two-stage model ages ( $T_{DM2}$ ) of 1.51 to 1.67 Ga. The tonalite sample has  $\epsilon_{Nd}(t)$  of  $-2.8$  and  $I_{Sr}$  of 0.7076 with  $T_{DM2}$  of 1.63 Ga. The granodiorite and MME exhibit  $\epsilon_{Nd}$  of  $-2.5$  to  $-3.9$  and  $I_{Sr}$  of 0.7075 to 0.7082 with  $T_{DM2}$  of 1.29 to 1.53 Ga, showing that their Sr–Nd isotopic features highly resemble (Fig. 7). Biotite monzogranite samples have  $\epsilon_{Nd}$  of  $-4.4$  to  $-6.2$  and  $I_{Sr}$  of 0.7097 to 0.7104, and a wide range of  $T_{DM2}$  from 1.37 to 2.63 Ga. Porphyritic biotite granite has moderate  $\epsilon_{Nd}$  of  $-2.2$  to  $-2.7$  and  $I_{Sr}$  of 0.7060 to 0.7065 and  $T_{DM2}$  of 1.11 to 1.12 Ga. Diorite (including dioritic dyke) samples have

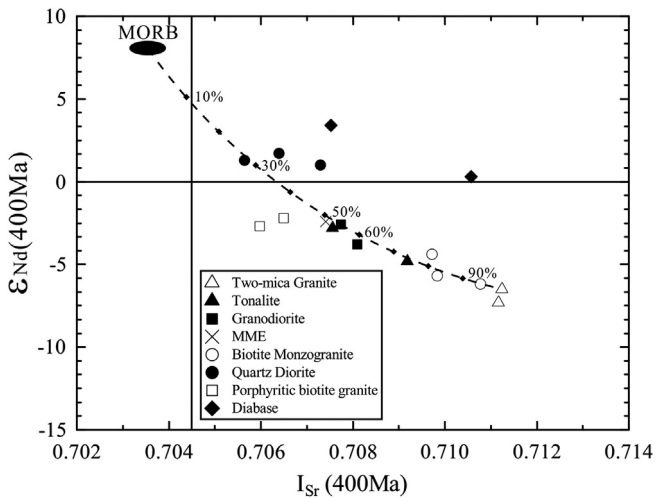


Fig. 7. Diagram of  $\epsilon_{\text{Nd}}(t)$  versus  $I_{\text{Sr}}$  for the intrusive rocks in the Dulan UHPM terrane. Composition of MORB used in binary mixing calculation is from Jahn et al. (1999).

the most positive  $\epsilon_{\text{Nd}}$  of 1.0 to 1.3 and  $I_{\text{Sr}}$  of 0.7056 to 0.7073 with a young  $T_{\text{DM2}}$  of 1.02 to 1.20 Ga.

#### 4.4. Zircon U–Pb geochronology

Eleven representative samples from several plutons were selected for zircon U–Pb age dating, including 07DL-01, 10DL-48 (two-mica granite), 10DL-44, 10DL-42 (tonalite), 07DL99, 07DL-79 (granodiorite), 07DL-78 (MME), 07DL-97 (biotite monzogranite), 07DL-102 (porphyritic biotite granite) and two samples (07DL-55 and 10DL-24) of diorite (Appendix Table 3).

Zircons from the two-mica granite (07DL-01, 10DL-48) are colorless, euhedral and prismatic crystals, ranging in length from 50  $\mu\text{m}$  to 250  $\mu\text{m}$  with axial ratios of about 1:1 to 3:1. Cathodoluminescent (CL) images show that most zircons retain clear core-rim structure; the rims show oscillatory zoning of magmatic origin and cores are inherited with complicated zoning (magmatic vs. metamorphic) (Fig. 8a). Twenty-four concordant analyses of sample 07DL-01 form four major age groups (Fig. 8a and b). The major magmatic group (group 1) ( $n = 10$ ) yields a weighted-mean  $^{206}\text{Pb}/^{238}\text{U}$  age of  $397 \pm 5$  Ma (MSWD = 1.2). Three cores (group 2) with unzoned or cloudy CL luminescence give a weighted mean  $^{206}\text{Pb}/^{238}\text{U}$  age of  $427 \pm 7$  Ma (MSWD = 0.66). Five magmatic cores with oscillatory bands (group 3) form a weighted mean  $^{207}\text{Pb}/^{206}\text{Pb}$  of  $937 \pm 48$  Ma (MSWD = 0.80); and the last three cores (group 4) give a weighted-mean  $^{207}\text{Pb}/^{206}\text{Pb}$  of  $1809 \pm 51$  Ma (MSWD = 0.54). Twenty-seven analyses in sample 10DL-48 are all concordant (Fig. 8c and d). Twenty analyses of clear magmatic origin form a  $^{206}\text{Pb}/^{238}\text{U}$  weighted mean age of  $404 \pm 4$  Ma (MSWD = 1.8), three analyses of zircon cores give a mean of  $444 \pm 8$  Ma (MSWD = 0.17), and other four cores yield ages of  $656 \pm 10$ ,  $814 \pm 12$ ,  $874 \pm 13$  and  $1578 \pm 23$  Ma, respectively.

Zircon separates from tonalite samples 10DL-44 and 10DL-42 are colorless, hexagonal bi-pyramids with long axes varying from 100  $\mu\text{m}$  to 250  $\mu\text{m}$  and length/width ratios from 1.5 to 3. For 10DL-44, twenty-two zircon grains have been subdivided into three groups (Fig. 8e): (1) relic cores with Precambrian ages, (2) zircon with a bright CL image and ambiguous zoning exhibit ages identical to metamorphism, and (3) zoned rims exhibit ages of magmatism. Sample 10DL-44 yields 22 concordant analyses mainly clustered into two groups with weighted-mean  $^{206}\text{Pb}/^{238}\text{U}$  ages of  $392 \pm 5$  Ma ( $n = 9$ , MSWD = 0.25) and  $423 \pm 6$  Ma ( $n = 6$ , MSWD = 0.11) (Fig. 8f). Four zircon cores give concordant  $^{206}\text{Pb}/^{238}\text{U}$  ages of 785–885 Ma, similar to some protolith ages of eclogites (Song et al., 2010, 2014a; Zhang et al., 2010). One core yields a Mesoproterozoic age of  $1537 \pm 23$  Ma.

Twenty-three analyses of 10DL-42 give a weighted-mean  $^{206}\text{Pb}/^{238}\text{U}$  age of  $391 \pm 4$  Ma (Fig. 9a).

Zircons from granodiorite samples 07DL-79 and 07DL-99 are euhedral crystals of 100–250  $\mu\text{m}$  showing clear magmatic origin without relic cores. Twenty-five concordant analyses of 07DL-99 yield a weighted-mean  $^{206}\text{Pb}/^{238}\text{U}$  age of  $386 \pm 2$  Ma (MSWD = 1.4) (Fig. 9b). Twenty concordant analyses of 07DL-79 yield a weighted-mean  $^{206}\text{Pb}/^{238}\text{U}$  age of  $379 \pm 2$  Ma (MSWD = 1.05) (Fig. 9c). Zircons from the MME sample (07DL-78) are euhedral crystals of 50–150  $\mu\text{m}$  with wide bands of oscillatory zoning. Twenty-four concordant analyses form a weighted-mean  $^{206}\text{Pb}/^{238}\text{U}$  age of  $380 \pm 3$  Ma (MSWD = 1.4) (Fig. 9d), which is identical to the age of the host granodiorite, a scenario as seen in plutons of East Kunlun orogenic belt (Huang et al., 2014).

Zircons from biotite monzogranite sample (07DL-97) are euhedral, but less transparent under microscope, possibly due to radiogenic damage caused by high abundance of uranium. They show dark luminescence with weak oscillatory zoning in CL images, which is in accordance with the high concentrations of U (95–8576 ppm), Th (80–4836 ppm) and REE concentration. Ten analyses give a concordant weighted mean  $^{206}\text{Pb}/^{238}\text{U}$  age of  $380 \pm 5$  Ma (MSWD = 3.1) (Fig. 9e).

Zircons collected from porphyritic biotite granite (07DL-102) are euhedral crystals and 100–300  $\mu\text{m}$  in size, they show clear oscillatory zoning in CL images. Twenty-two analyses form a weighted-mean  $^{206}\text{Pb}/^{238}\text{U}$  age of  $367 \pm 3$  Ma (MSWD = 1.6) (Fig. 9f).

Zircons from dioritic dyke sample 07DL-55 and diorite sample 10DL-24 are colorless and show transparent cracks with original lengths possibly exceeding 200  $\mu\text{m}$ . In the CL image they maintain wide bands of oscillatory zoning without clear core-rim structure. Sample 07DL-55 yields 13 concordant analyses with a weighted-mean  $^{206}\text{Pb}/^{238}\text{U}$  age of  $360 \pm 4$  Ma (MSWD = 2.5) (Fig. 9g). Twenty-five analyses of 10DL-24 are concordant and yield a weighted-mean  $^{206}\text{Pb}/^{238}\text{U}$  age of  $374 \pm 2$  Ma (MSWD = 1.03) (Fig. 9h).

#### 4.5. Zircon Hf isotope

Zircon  $\epsilon_{\text{Hf}}(T)$  histograms for all samples except MME are shown in Fig. 10. For detailed results, see Appendix Table 4. For two-mica granite samples, analyses of non-inherited zircons give  $\epsilon_{\text{Hf}}(T)$  values of  $-5.1$  to  $3.2$  (peaked at  $-3.1$ ) and two-stage Hf model ages ( $T_{\text{DM2}}$ ) of 1.19–1.72 Ga. Zircons from the tonalite give a wide range of  $\epsilon_{\text{Hf}}(T)$  of  $-8.5$  to  $7.0$  (peaked at 1.4) and  $T_{\text{DM2}}$  of 1.50–2.50 Ga. Zircon  $\epsilon_{\text{Hf}}(T)$  of the granodiorite distributes between  $-5.2$  and  $0.0$  (peaked at  $-2.2$ ), and  $T_{\text{DM2}}$  between 1.38 and 1.72.  $\epsilon_{\text{Hf}}(T)$  of the biotite monzogranite distributes between  $-5.5$  and  $-0.2$  (peaked at  $-2.1$ ), and  $T_{\text{DM2}}$  between 1.39 and 1.73. For the porphyritic biotite granite, the distribution of  $\epsilon_{\text{Hf}}(T)$  values is relatively scattered between  $-5.5$  and  $2.8$  (peaked at 2.0) and  $T_{\text{DM2}}$  between 1.19 and 1.67. Diorite and dioritic dyke samples have positive  $\epsilon_{\text{Hf}}(T)$  values of 2.2 to 11.9 (peaked at 5.8) with  $T_{\text{DM}}$  between 0.53 and 0.93 Ga.

## 5. Discussion

### 5.1. Petrogenesis of the Shaliuhe granitoid complex: multi-stage of exhumation of subducted continental crust

#### 5.1.1. Two-mica granite—melting of the exhumed upper crust

As illustrated above, the two-mica granite shows characteristics of S-type signature in terms of both mineral assemblage and peraluminous composition. The genesis of S-type granite can be attributed to either pure crustal melting, or hybridization of multiple magmas (Chen et al., 2014; Douce, 1995, 1999; Douce and Beard, 1995). In the former scenario, it could be generated by melting of pelites, or immature crustal sources, i.e. metagraywackes and metagneous, or melting of metaluminous rocks with or without subsequent fractional crystallization (Auzanneau et al., 2006; Chen et al., 2014; Douce and Beard, 1995; Douce and Johnston, 1991; Miller, 1985; Montel and Vielzeuf,

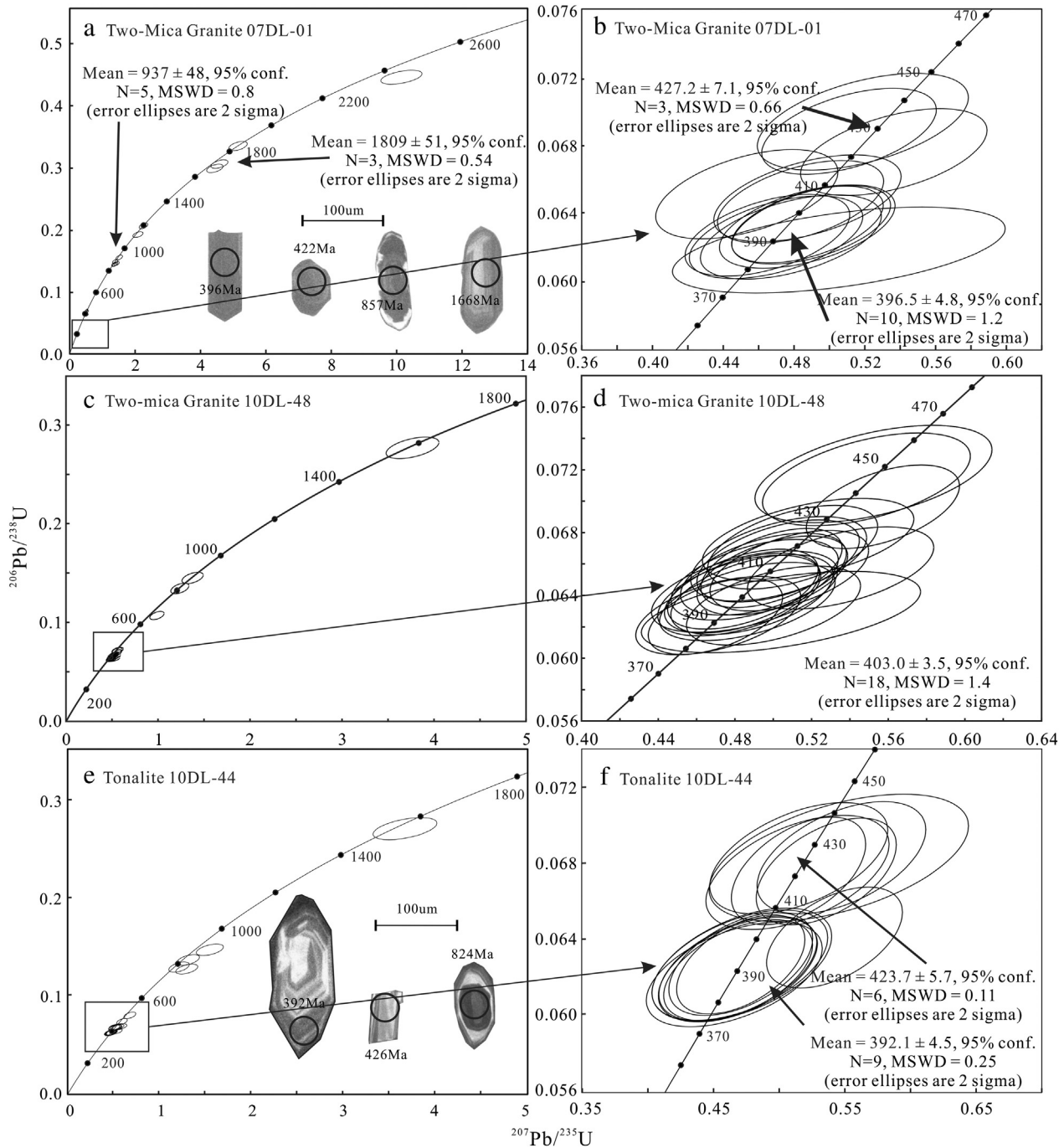


**Fig. 8.** LA-ICP-MS Concordia of zircon U–Pb isotope analyses for two-mica granite 07DL01 (a and b), two-mica granite 10DL-48 (c and d), and the tonalite 10DL-44 (e and f), together with representative zircon CL images.

1997; Vielzeuf and Montel, 1994). The high-silica characteristics of the two-mica granite and the absence of MME or xenoliths indicate that both magma mixing and assimilation–fractional crystallization, if occurring, cannot be the dominant processes. Fractional crystallization is unlikely due to: (1) the lack of intermediate or mafic equivalent, and (2) the chemical homogeneity of the two-mica granite, which suggest minor magma differentiation. As illustrated in Figs. 7 and 8, the two-mica granite samples have REE and trace element patterns resembling those of the average Qaidam basement rocks (Wan et al., 2006), suggesting a possible link between them. Using the discrimination diagrams proposed by Sylvester (1998), high  $\text{CaO}/\text{Na}_2\text{O}$  ( $>0.47$ ) and  $\text{Al}_2\text{O}_3/\text{TiO}_2$  (62–65), low  $\text{Rb}/\text{Ba}$  (0.23–0.29) and  $\text{Rb}/\text{Sr}$  (0.92–1.21) of the two-mica granite are indicative of a clay-poor source with low-

degree partial melting (Fig. 11). Additionally, the slight elevation of  $\epsilon\text{Nd}$  of the two-mica granite ( $-6.6$  to  $-7.3$ ), compared to those of the bulk Qaidam–Qilian basement ( $-7.7$  to  $-13.9$ , Wan et al., 2006, recalculated to 400 Ma), may imply a mild alteration by melts with radiogenic Nd isotopic signature.

Exhumation of the North Qaidam UHP rocks has been constrained to ca. 410–400 Ma, about 10–20 m.y. after peak metamorphism (Chen et al., 2009; Mattinson et al., 2006a; Song et al., 2005, 2006; Zhang et al., 2010). For the two-mica granite, the two weighted mean ages of  $397 \pm 5$  Ma and  $404 \pm 4$  Ma represent the timing of magma crystallization. These ages are also identical within error to the age of exhumation. More importantly, the age frame of inherited zircon in the two-mica granite, which mainly consists of inherited metamorphic zircon cores

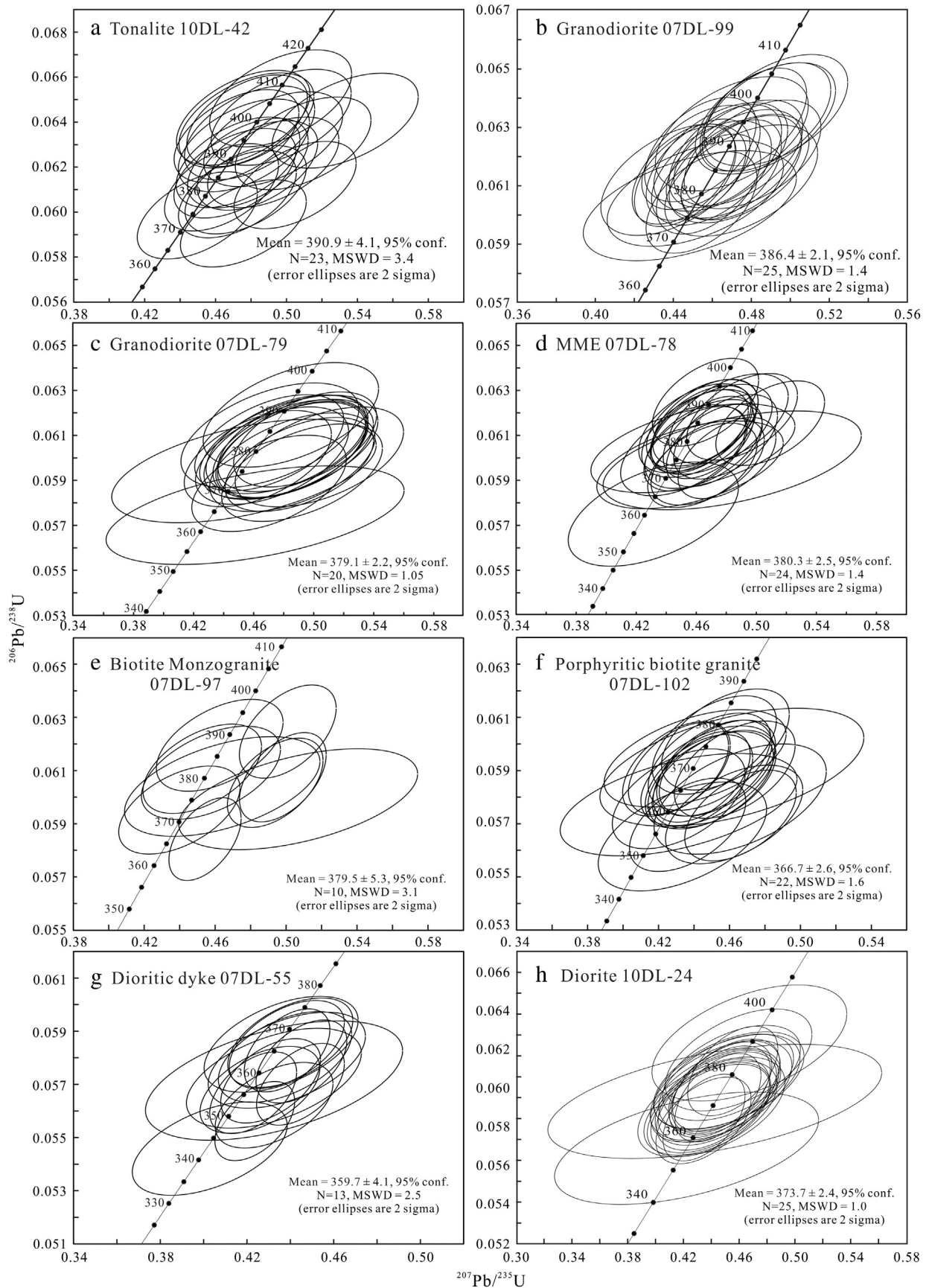


**Fig. 9.** LA-ICPMS Concordia of zircon U–Pb isotope analyses for (a) tonalite 10DL-42, (b) granodiorite 07DL-99, (c) granodiorite 07DL-79, (d) MME 07DL-78, (e) biotite monzogranite 07DL-97, (f) porphyritic biotite granite 07DL-102, (g) diorite 07DL-55, and (h) diorite 10DL-24.

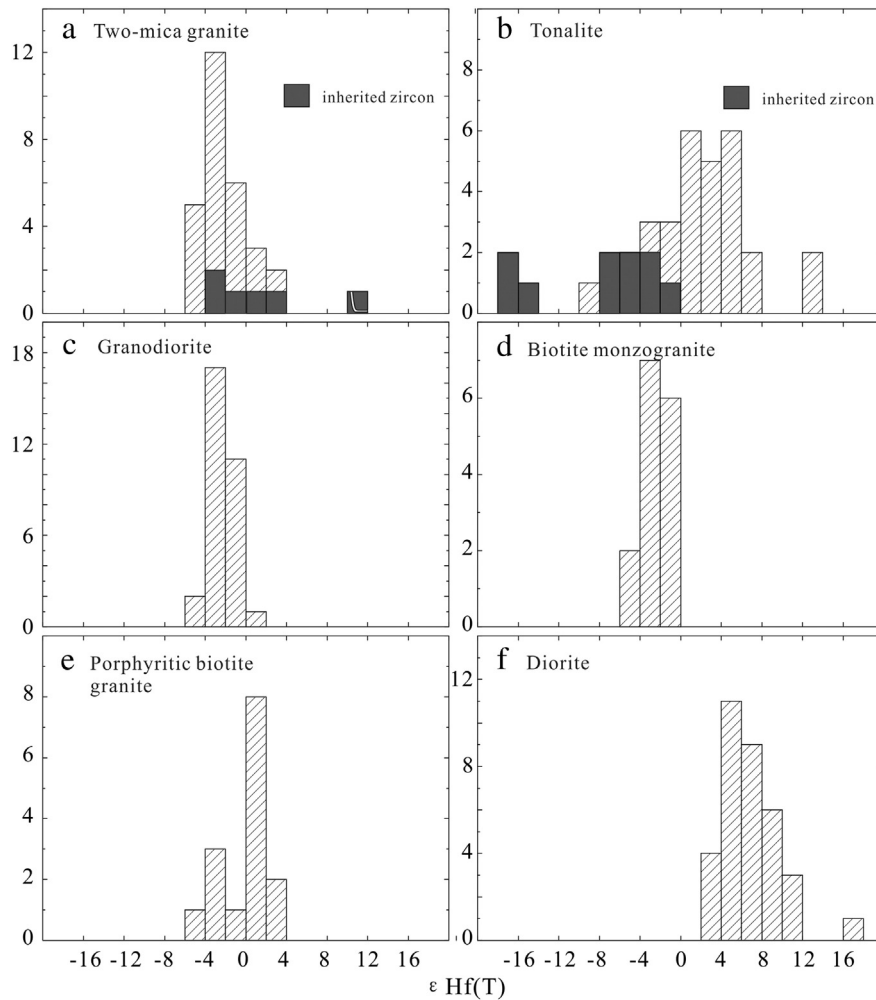


Fig. 10. Zircon  $\epsilon_{\text{Hf}}(\text{T})$  histograms for the intrusive rocks in the Dulan UHPM terrane.

of 427–433 Ma, minor Neo- and Paleo-Proterozoic zircon cores of  $937 \pm 48$  Ma ( $n = 5$ ) and  $1809 \pm 51$  Ma ( $n = 3$ ), resembles those major UHP metamorphic ages and protolith ages of the North Qaidam UHPM belt, respectively (Mattinson et al., 2006b, 2009; Song et al., 2006, 2012, 2014a, 2014b). Combining the geochemistry with the integrated zircon age spectrum, we interpret the two-mica granite as syn-exhumation magma that is most likely the product of melting of the UHP metamorphosed Proterozoic gneissic basement of the North Qaidam UHP belt (Fig. 12).

#### 5.1.2. Tonalite—melting of exhumed lower mafic crust?

Compositionally, the tonalite differs distinctly from adakite (high-Al TTG) due to its low Sr, high Y and HREE, although their mineralogy and major elements share great similarity. The relatively flat REE pattern (Fig. 5b) shows that garnet cannot be a restite phase in the source. The tonalite yields zircon U–Pb age of  $392 \pm 5$  Ma. Notably, it maintains inherited zircon ages resembling that of the two-mica granite (Fig. 9), indicating participation of Proterozoic basement of the Qaidam block in magma genesis. The inherited zircons maintain highly varied  $\epsilon_{\text{Hf}}(\text{T})$  from  $-1.8$  to  $-17.6$ , indicating that the tonalite may have been derived from remobilized old basement. Besides, as the  $\text{K}_2\text{O}/\text{Na}_2\text{O}$  ratio of tonalitic melts is a function of the source composition during dehydration melting (Beard and Lofgren, 1991), as well as the low  $\text{SiO}_2$  (56–66 wt.%), the tonalite is likely derived from a mafic, sodium-rich source. In contrast to the granodiorite, no evidence for hybridization is observed in the tonalite. The remarkably low Cr (2–95 ppm, mostly <25 ppm) and Ni (1.7–10 ppm) implies that this tonalite

magma may have been directly derived from mafic lower crust without injection of mantle materials. Therefore, we conclude that the tonalite results from high-degree melting of mafic crustal material of the North Qaidam UHP belt, e.g. the subducted lower continental crust, under low-pressure conditions, shallower than the garnet stability field, corresponding to a depth of less than 30 km.

#### 5.2. Petrogenesis of the Yematan granitoid complex: contributions of mantle and magma mixing

As shown in Fig. 1d, the Yematan granitoid complex contains various rock types of varying nature. These rocks, on the basis of age data, represent an event spanning ~30 Mys, from granodiorite and biotite monzogranite at 386–379 Ma, porphyritic biotite granite at 367 Ma, to diorite at 374–360 Ma.

##### 5.2.1. MME-hosting granodiorite and biotite monzogranite—hybrid magma?

The granodiorite with I-type affinities is clearly different from the local crustal melts represented by the two-mica granite and tonalite. The distinct features of granodiorite include: (1) lower  $\text{SiO}_2$  and alkali elements with high  $\text{Na}_2\text{O}/\text{K}_2\text{O}$  ratios (>1); (2) low total REE, slight LREE enrichment with a negative Eu anomaly; (3) relatively low  $I_{\text{Sr}}$  and slightly negative  $\epsilon_{\text{Nd}}$ ; (4) high modes of mafic minerals; and (5) the presence of a large quantity of MME and mafic dykes. The abnormal plagioclase zoning and coeval MME indicate clearly that the granodiorite cannot be formed simply by fractional crystallization of

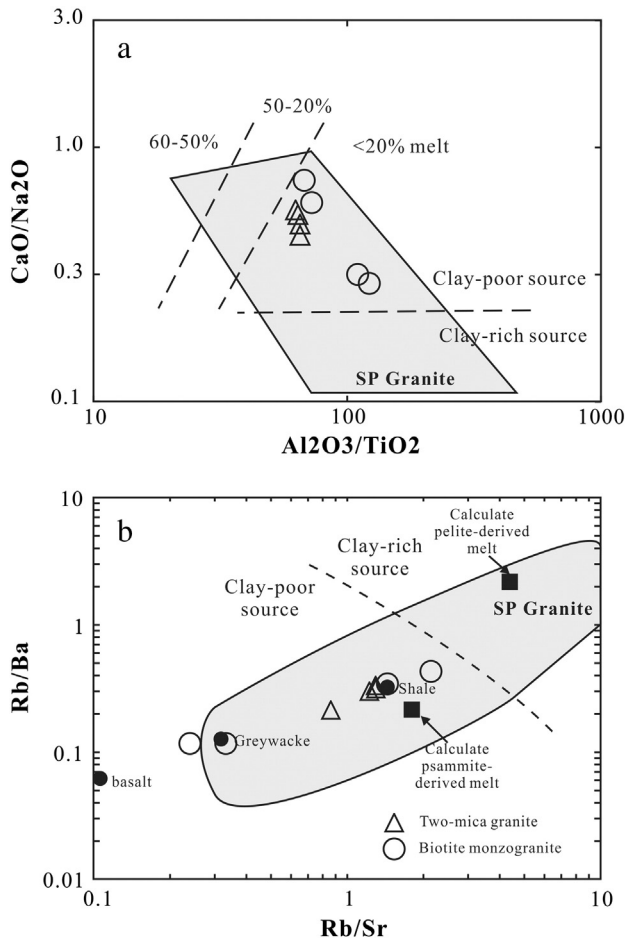


**Fig. 11.** (a) CaO/Na<sub>2</sub>O versus Al<sub>2</sub>O<sub>3</sub>/TiO<sub>2</sub> diagram for the two-mica granite and biotite monzogranite. (b) Rb/Ba versus Rb/Sr diagram for the two-mica granite and biotite monzogranite.

Modified from Sylvester (1998).

melts from either lower continental crust or lithospheric/asthenospheric mantle (e.g. Liégeois et al., 1998; Roberts and Clemens, 1993). Mixing of either two different magmas (e.g. Chen et al., 2002; Collins, 1996), or early crystallized cumulates in periodically replenished magma chamber (e.g. Huang et al., 2014), could possibly explain the genesis of MME in the granodiorite. In the former scenario, the MMEs represent quenched mafic melts during successive injection, which is also supported by the presence of textural and compositional disequilibrium in the minerals of MME. The major problem is the equivalent isotopic signatures between MME and its host granodiorite (Figs. 7 and 10).

The coeval biotite monzogranite occurs intimately associated with granodiorite, and it also contains MME. The mafic enclaves show fine-grained texture with less plagioclase, suggesting rapid quenching and less mass exchange between the intruded mafic melts and the host felsic granite (Barbarin, 2005). The contrast between biotite monzogranite and enclaves implies that these enclaves, rather than those hosted by granodiorite, are likely to represent mafic blobs formed during injection of mafic magma. Such injection of mafic magma may occur before the felsic magma completely crystallized. The variable  $\epsilon_{\text{Nd}}(T)$  values from  $-6.2$  to  $-4.4$  of three biotite monzogranite samples thus could be attributed to a progressive alteration of mafic magma (Fig. 7). It can be seen from REE patterns (Fig. 6d) that biotite monzogranite might have been altered to a different extent by mafic melts.

The combination of coeval granodiorite, MMEs, diabase dykes, and MME-hosting biotite monzogranite fits well into the scenario described by Barbarin (2005), which indicated that MME-host I-type granitoids

could be produced by thorough mixing of mafic and felsic magma. We perform a binary-mixing calculation to test the possibility of magma-mixing origin of the granodiorite. We use the parental magma of biotite monzogranite as the felsic end member, considering (1) it is concurrent with granodiorite, and (2) it has clear crustal feature. As illustrated by Fig. 7, mixing calculation using depleted mantle basalts ( $\text{Sr} = 119.8$  ppm,  $\text{Nd} = 7.6$  ppm,  $I_{\text{Sr}}(400 \text{ Ma}) = 0.70355$ ,  $\epsilon_{\text{Nd}}(400 \text{ Ma}) = 7.5$ ) and the least-altered biotite monzogranite sample could well achieve the isotopic signature of granodiorite, by mixing of 40–50% crustal melts with depleted mantle melts. This result is also compatible with the same binary calculation using most major elements of the two end-members.

In this regard, it is possible that the granodiorite is the hybrid magma through mixing of crustal- and mantle-derived magma. The MMEs in the granodiorite could either represent quenched mafic melts or autolith from disruption of early cumulates. Biotite monzogranite represents coeval crustal magma slightly altered by mantle melts. The mafic dykes and MMEs hosted by biotite monzogranite most likely represent the least-altered mantle melts. In addition, unlike the earlier two-mica granite/tonalite, the granodiorite and biotite monzogranite, as well as the porphyritic biotite granite do not show any mineral orientation, suggesting an extensional setting without strain when they emplaced and crystallized.

### 5.2.2. Porphyritic biotite granite—melting of amphibolite at low pressure?

The 367 Ma porphyritic biotite granite spans a relatively large compositional range of SiO<sub>2</sub> (68.76–73.37 wt.%) and K<sub>2</sub>O/Na<sub>2</sub>O ratios (0.52–1.71) that are different from previous granites. Perthite is ubiquitous in the porphyritic biotite granite and suggests high magma temperature. The enriched LREE patterns with depleted MREEs and elevated HREEs (Fig. 5e) are indicative of a hornblende-bearing, garnet-free residuum, pointing to a low-pressure residual assemblage after partial melting of mafic or intermediate source, which is compatible with melt compositions of 10%, 20% and 30% accumulated fractional melting from amphibolite of upper oceanic crust (UOC) composition (75% average N-MORB and 25% average E-MORB) (Niu and O'Hara, 2009). Note that some porphyritic biotite granite samples with high Sr content (325–409 ppm) and high Sr/Y ratio (24–30) do not mean that they are real adakite, but indicate a tonalitic or adakitic source under middle or lower crust condition (Kamei et al., 2009).

The relatively young Nd model age (1.07–1.12 Ga) and low Rb/Sr ratio (0.19–0.44) exclude the possibility of the old continental crust as a source of porphyritic biotite granite. In conclusion, porphyritic biotite granite may form by partial melting of a juvenile crustal component under high-temperature, low-pressure (amphibole stability field?) conditions, consistent with the Grenville-age protolith of the UHPM belt (e.g. Song et al., 2012).

### 5.2.3. Diorite—mantle magmas with crustal contamination by extension

The 373–360 Ma mafic-to-intermediate magma with SiO<sub>2</sub> of 52–60 wt.% generally implies either a mafic crustal source with high degrees of partial melting, or a mantle source. According to the experiments by Rapp and Watson (1995), metaluminous intermediate melts generated through dehydration melting of mafic rocks are marked by low MgO (<3.2 wt.%) and Mg# (<38). However, geochemical signatures of diorite, including high contents of MgO (4.05–6.81 wt.%), Mg# (64–71) and compatible elements (Cr, up to 247 ppm, Ni, up to 56 ppm), preclude the possibility of a crustal derivation.

Compared to typical melts of mantle peridotite (e.g., Falloon et al., 1988; Hirose and Kushiro, 1993), diorite exhibits higher SiO<sub>2</sub> and Al<sub>2</sub>O<sub>3</sub> as well as lower TiO<sub>2</sub>, MgO and Fe<sub>2</sub>O<sub>3</sub>. Its slightly positive  $\epsilon_{\text{Nd}}(T)$  (1.0 to 1.7) and relatively high  $I_{\text{Sr}}$  (0.7056 to 0.7073), combined with the mild enrichment in LREE, LILE and depletion in Nb, P, and Ti, could result from partial melting of enriched lithospheric mantle with subsequent fractional crystallization (e.g. Altherr et al., 2000). Niu et al. (2013) argued that although melting of wet mantle peridotite

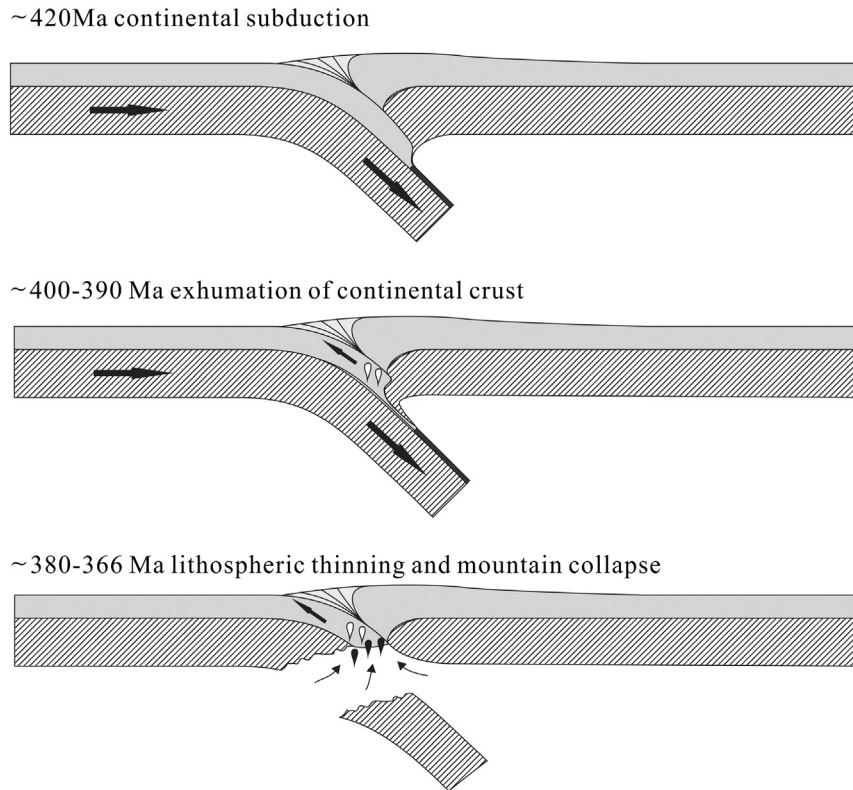


Fig. 12. Cartoon for post-collisional evolution of the North Qaidam UHP belt.

could produce high-Mg andesitic melts (Hirose, 1997; Kushiro et al., 1968; O'Hara, 1965), the amount of melt produced is too tiny (<1% mass fraction) compared to huge granitoids. Of our samples, the enriched isotopic and geochemical signatures may have been disturbed by crustal contamination so as not to reflect the nature of its source (e.g. Paquette et al., 2003). The relatively diffusive Sr isotope (Fig. 7), for instance, cannot be acquired by fractional crystallization, but more likely results from contamination of continental crust to various extents. Moreover, local crustal-derived magma, including two-mica granite and biotite monzogranite, exhibits similar  $\text{Na}_2\text{O}$  contents to the most mafic diorite samples, while their  $\text{K}_2\text{O}$  contents are much higher, thus progressive bulk assimilation of mantle magma by crustal rocks would lead to negligible change in  $\text{Na}_2\text{O}$  but a significant increase in  $\text{K}_2\text{O}$ .

In addition,  $T_{\text{DM}}$  of diorite calculated from zircon Hf isotopic ratios ranges between 0.53 and 0.93 Ga, suggesting a juvenile, depleted mantle source. Therefore, the 373–360 Ma diorite is likely to be derived from depleted asthenospheric mantle with subsequent crustal alteration during the post-orogenic extension, which marks the end of the whole orogenic cycle.

### 5.3. Decompression melting during exhumation of decoupled continental crust

It is generally thought that slab breakoff is the trigger for exhumation of UHP rocks in UHPM belts worldwide. In the scenario of slab breakoff, upwelling of hot asthenospheric mantle leads to thermal perturbation of the metasomatized overriding lithosphere, gives rise to mantle-derived magma, which underplates in an upper plate consisting of subducted continental crust and causes crustal melting and genesis of collision-related granitoids (Davies and von Blanckenburg, 1995). Alternatively, exhumation of the continental crust could also be syn-convergent, initiated by crust–mantle decoupling in a syn-collisional setting as a consequence of increasing positive buoyancy against the

drag force of the underlying mantle (e.g. Chemenda et al., 1995; Labrousse et al., 2011; Song et al., 2014a).

The Shaliuhe granitoid complex, including the two-mica granite and tonalite as described above, consists crust-derived magmas with negligible mantle alteration. It is different from typical slab-breakoff magmatism due to the lack of mantle-derived magmatism in the area (e.g. Atherton and Ghani, 2002; Whalen et al., 2006). Additionally, the intrusive rocks were emplaced in the deeply subducted continental crust (the UHP metamorphic complex), while slab break-off predicts emplacement of magma in the supra-subduction-zone lithosphere.

Breakoff-induced exhumation of the continental crust from mantle depths towards shallower levels, on the other hand, will lead to decompression of UHP metamorphic rocks. Partial melting can be triggered during decompression, an important mechanism for the genesis of crust-derived magmas (e.g. Song et al., 2014b; Whitney et al., 2004), which in turn reflects the characteristics of the source and process. Studies have reported thermal relaxation of UHP rocks in the Dulan terrane, which leads to a temperature increase from ~700 °C to over 900 °C after peak metamorphism, corresponding to a high-pressure-granulite-facies overprint (Song et al., 2003a,b). Such relaxation is followed by an amphibolite-facies retrogression at ~400 Ma (Song et al., 2006). According to an experimental study (e.g., Auzanneau et al., 2006), decompression melts of felsic continental crust under high pressure compositionally resemble our two-mica granite, e.g. high contents of  $\text{SiO}_2$  and  $\text{K}_2\text{O}$  as well as medium  $\text{Al}_2\text{O}_3$  and CaO. The reaction involving phengite breakdown during retrogressive eclogite/amphibolite phase transition, which occurs at 2.0–2.3 GPa and 800–900 °C, might be responsible for the genesis of the two-mica granite (Auzanneau et al., 2006). Therefore, subducted felsic crust dominated by 900–1000 Ma age zircons is most likely the source of the two-mica granite.

The tonalite, on the other hand, has a different source composition from the two-mica granite. All geochemical features, including whole-rock compositions, Sr–Nd and zircon Hf isotopes, suggest that the

tonalite was derived from partial melting of mafic lower crust at depths shallower than the garnet stability field. The age gap of ~5 Ma may also imply a discrepant exhumation of mafic crustal component following the upward movement of the upper continental crust.

Consequently, the two-mica granite and tonalite in the Shaliuhe granitic complex may result from successive exhumation of decoupled slices of continental crust. Slow exhumation of continental crust with the aid of upwelling mantle could generate granitic melts with S-type signature by melting of upper felsic crust and tonalite melt by melting of lower mafic crust. Similar exhumation models of multi-slice successive exhumation have been previously proposed for other UHP continental collision zones (e.g. Dabie–Sulu orogen in China, Li et al., 2009; Liu and Li, 2008), and have been modeled numerically using detailed thermal and tectonic constraint (e.g. Warren et al., 2008; Yamato et al., 2008) so as to provide insights into the features of exhumed continental crust after UHP metamorphism.

#### 5.4. Magmatism in association with unrooting (extension) and mantle-crustal interaction during orogen collapse

Regional stratigraphic constraints, e.g. a transition from thick Devonian molasse to early-Carboniferous cover in the Qilian–Qaidam comprehensive orogenic system, indicate a collapse of the North Qaidam belt following the early-Devonian mountain building uplift (Song et al., 2013). This implies termination of continental subduction and a transition in tectonic regime from compression to extension, which coincides with our documentation of post-collisional magmatic activity. The emplacement of the Yematan granitoid complex occurred at ca. 386–380 Ma, revealing that the magmatism is in correspondence to the extensional collapse, whose impact on triggering magma genesis lasted to ca. 360 Ma, the end of Devonian. The contemporaneous mafic dykes (~390–360 Ma) within granodiorite and diorite intrusions testify to the extension and asthenosphere upwelling. Extension of the orogenic lithosphere is often ascribed to slab breakoff or delamination of an orogenic root, convective removal of thermal boundary layer, or detachment of the lower part of the lithosphere (Bird, 1979; Davies and von Blanckenburg, 1995; Houseman et al., 1981), all of which predict magmatism with distinct characteristics. It is, however, difficult to distinguish among different models solely by geochemical and isotopic results (e.g. Miller et al., 1999). More frequently, these results are combined with temporal and spatial associations, and evolutionary trends of collapse magmatism to examine the match of each model (e.g. Turner et al., 1999; Whalen et al., 2006).

The erosion (denudation or delamination) of the mountain root after slab breakoff could be the cause of orogen collapse and further lithosphere extension. This tectonic scenario should be capable of explaining the following characteristics of long-term crust–mantle interaction in the North Qaidam belt: (1) Diachronous emplacement of the magmas. The ca. 25 m.y. magmatic events during orogen collapse began at ca. 386 Ma with the volumetrically dominant biotite monzogranite and granodiorite, and terminated at ca. 360 Ma with more mafic diorite. (2) Compositional evolution trends of magmas as an indicator of interaction between mantle and crust in post-collisional magmatism. The systematic elevations in  $\epsilon_{\text{Nd}}(\text{T})$  and  $\epsilon_{\text{Hf}}(\text{T})$  of plutons from ca. 386 to 360 Ma (Figs. 7 and 10) provide evidence for an increasing contribution from a depleted mantle source. Mantle melts are formed at the end of the orogen collapse at ca. 360 Ma, as represented by the diorite pluton. (3) The interaction between the asthenosphere and the Qaidam UHPM gneisses confirmed by contemporaneous melting of felsic crust and the asthenosphere and mixing of these two melts.

Therefore, convective thinning and delamination of the continental lithospheric mantle after slab breakoff are able to explain the massive occurrence of depleted mantle melts. In both models, removal of the lithospheric mantle leads to a rapid enhancement in regional thermal gradient as well as uplift and subsequent collapse of the continental surface (e.g. Nelson, 1992; Turner et al., 1999), which is consistent

with the stratigraphic evidence for the post-collisional orogen collapse in the North Qaidam belt. It should be noted that decompression melting of the asthenosphere requires a shallow upwelling to the asthenosphere to less than 50 km (Davies and von Blanckenburg, 1995). This could be more readily explained as a consequence of delamination of the entire lithospheric mantle, rather than convective erosion of its root. Additionally, the presence of massive crustal melts also argues for lithospheric delamination (e.g. Collins, 1994; Kay and Mahlburg Kay, 1993).

The distinctive evolution trend of the magmatism after ca. 386 Ma does not fit well with a delamination magmatic model, which would produce a one-way transition from dominantly mantle-derived to crustal-derived magma. This is possibly the result of simultaneous progressive extension and mantle upwelling. Shortly after the onset of delamination, underplating of the mafic magma beneath continental crust triggered crustal melting, leading to subsequent production of crustal-derived melts. Extensive mixing between mafic and felsic magmas could produce hybrid magma, e.g., granodiorite. This requires long durations of interaction of melts at deep crustal levels (e.g. Yang et al., 2005). With respect to the progressive extension, mafic melts are able to transfer upward as dykes, gather together and form mafic magma chambers. This would reduce the extent of melt interaction, giving rise to diorite that is relatively primitive, retaining a more mantle-like signature.

The entire process, from the emplacement of the exhumation-induced two-mica granite/tonalite to the later crustal- and mantle-derived magmas after removal of lithospheric mantle, provides a good example for post-collisional magmatism in an UHPM belt. One of the striking features of our study is the rapid transition from exhumation of continental crust, or crust–mantle decoupling, to the later extension of orogen. The Dulan two-mica granite at the early stage is equivalent to the exhumation-induced melting in French Massif Central with the age of 390–370 Ma (Faure et al., 2008). The latter has a significant, 30–50 Mys gap to the later collapse magmatism. Exhumation magmatism in Sulu orogen also predates the later post-collisional magmatism by ~80–100 Mys (He et al., 2011; Xu et al., 2007; Zhao et al., 2011, 2012). In Dulan, however, collapse magmatism occurred closely after the emplacement of crustally derived magmas. Possible reasons include (1) difference in crust architecture, and (2) different retrogressive P–T paths for the exhumed UHP continental crust.

Collapse magmatism in Dulan is active over a ~30 Mys time span, and contains various transtensional, undeformed lithologies. It is comparable to the post-collisional magmatism in European Variscides (e.g. Altherr et al., 2000; Dias et al., 1998; Faure et al., 2010; Paquette et al., 2003) and Caledonides (Atherton and Ghani, 2002). An increasing mantle input is observed during North Qaidam orogenic collapse, which leads to the generation of early granodiorite representing crust–mantle interaction, and the later mantle-derived diorite. Similar feature is also observed in Corsica–Sardinia (Paquette et al., 2003; Renna et al., 2006).

## 6. Conclusion

Post-collisional magmatism in the Dulan UHP terrane is highly diverse in age and composition, indicating multi-stage and various sourced melting and interaction between crust and mantle associated with a complex tectonic evolution from exhumation to orogen collapse. Magmatism started with melting of different layers of the Qaidam continental crust at ca. 404–391 Ma, followed by participation of mantle at ca. 386 Ma with intensive crust–mantle interaction, and large-scale decompression melting of the asthenosphere lasted to ca. 360 Ma. Table 1 summarizes characteristics of these plutons.

Post-collisional magmatism in the North Qaidam UHPM belt occurred ~20–30 Mys later than peak UHP metamorphism (>420 Ma) during continental collision, and lasted for an over 40 m.y. time span till the end of the orogenic cycle. These magmas vary significantly due

**Table 1**  
Compilation of the plutonic rocks in the Dulan terrane of the N. Qaidam UHPM belt.

	Shaliuhe granitoid complex		Yematan granitoid complex		Diorite	Diabasic dyke
	Two-mica granite	Tonalite	Granodiorite	Biotite monzogranite		
Outcrop area (km <sup>2</sup> )	7	8	8	10	10	-
Number of sample	4	4	9 (including 3 MME samples)	6	4	3
MME presented?	×	×	✓	✓	×	-
Dyke presented?	×	×	Diabasic	Diabasic	Diabasic	-
Mineral assemblage	Mus + Bi + Pl + Kfs + Qz	Bi + Pls + Kfs + Qz	Hb + Bi + Pl + Kfs + Qz	Bi + Pl + Kfs + Qz ± Hb	Hb + Pl + Kfs ± Qz	Cpx ± Hb + Pl
Rock deformation	Weakly foliated	Moderately foliated	Massive	Massive	Massive	Massive
U-Pb age (Ma)	404–397	392–391	386–379	380	374–360	0.75–0.93
ASI	1.03–1.16	1.02–1.12	0.90–0.98	1.05–1.18	0.69–0.86	62–65
Mg#	35–36	48–56	51–56	25–44	64–71	3.4
Whole rock $\epsilon_{Nd}(T)$	-6.6 to -7.3	-2.8	-2.5 to -3.9	-4.4 to -6.2	1.0–1.3	-
Zircon $\epsilon_{Hf}(T)$ (in parentheses)	-5.1–3.2 (-3.1)	-8.5–7.0 (1.4)	-5.2–0.0 (-2.2)	-5.5 to -0.2 (-2.1)	2.2–11.9 (5.8)	-
shows peak value						
Possible explanation for petrogenesis	Partial melting of UCC	Partial melting of LCC	Mixing between melts from UCC and mantle	Representing crustal melts in magma mixing	Partial melting of juvenile depleted mantle	

to differences in sources and processes of formation. Magmatism during and after the exhumation of the UHP rocks in the North Qaidam belt are summarized below as regards their petrogenesis and associated tectonic evolution:

- (1) ~404–390 Ma: two distinct types of magma, including weakly-to-strongly peraluminous two-mica granite and the tonalite, intruded the UHP gneissic basement of the NDB. Both of the two magmatic rock types have similar inherited zircon age spectrum, while they are different in chemical and isotopic composition, indicating that they are partial melts of different levels of continental crust during exhumation. Such melting could have resulted from slab breakoff induced exhumation. A multi-slice, successive exhumation model for decoupled upper and lower crust could account for the formation of the two-mica granite and the tonalite; that is, the two-mica granite was most likely derived from the upper continental crust, whereas the tonalite might have a lower continental crust origin.
- (2) ~386–373 Ma: The involvement of asthenospheric mantle melts, as indicated by magma mixing and the genesis of granodiorite, resulted from unrooting/delamination of the entire lithospheric mantle. The coeval biotite monzogranite represents the crustal end-member in magma mixing. Relatively complete mixing of melts may reflect long-lived and substantial interaction between crust and mantle, possibly a feature of magmatism at the early stage of mantle upwelling, when orogenic extension still remained at a relatively low rate.
- (3) 373–360 Ma: diorite with mafic dykes represents asthenospheric mantle melting with less crustal contamination compared to granodiorite. Increasing mantle-derived magma is likely due to extension and mantle upwelling having reached its maximum extent. The large-scale mantle magmatism marks the final stage of the orogenic cycle.

Supplementary data to this article can be found online at <http://dx.doi.org/10.1016/j.lithos.2014.10.006>.

## Acknowledgments

We thank K.J. Hou and C.L. Guo for MC-ICP-MS in-situ zircon Hf analyses, and J.S. Wang, G.Z. Li, and W.P. Zhu for Sr–Nd isotopic analyses. We also thank the two anonymous official peer-reviewers and editors for their detailed and constructive comments. This study was supported by the Major State Basic Research Development Program (2015CB856105), the National Natural Science Foundation of China (Grant Nos. 41372060, 40825007, 41121062, 41130314) and Basic geological survey program of China Geological Survey (1212011121258).

## References

- Atherton, R., Holl, A., Hegner, E., Langer, C., Kreuzer, H., 2000. High-potassium, calc-alkaline I-type plutonism in the European Variscides: northern Vosges (France) and northern Schwarzwald (Germany). *Lithos* 50, 51–73.
- Andersen, T., 2002. Correction of common lead in U–Pb analyses that do not report <sup>204</sup>Pb. *Chemical Geology* 192, 59–79.
- Atherton, M., Ghani, A., 2002. Slab breakoff: a model for Caledonian, Late Granite syn-collisional magmatism in the orthotectonic (metamorphic) zone of Scotland and Donegal, Ireland. *Lithos* 62, 65–85.
- Auzanneau, E., Vielzeuf, D., Schmidt, M., 2006. Experimental evidence of decompression melting during exhumation of subducted continental crust. *Contributions to Mineralogy and Petrology* 152, 125–148.
- Barbarin, B., 1999. A review of the relationships between granitoid types, their origins and their geodynamic environments. *Lithos* 46, 605–626.
- Barbarin, B., 2005. Mafic magmatic enclaves and mafic rocks associated with some granitoids of the central Sierra Nevada batholith, California: nature, origin, and relations with the hosts. *Lithos* 80, 155–177.
- Beard, J.S., Lofgren, G.E., 1991. Dehydration melting and water-saturated melting of basaltic and andesitic greenstones and amphibolites at 1, 3, and 6.9 kb. *Journal of Petrology* 32, 365–401.
- Bird, P., 1979. Continental delamination and the Colorado Plateau. *Journal of Geophysical Research* 84, 7561–7571.

- Blanckenburg, F.v., Davies, J.H., 1995. Slab breakoff: a model for syncollisional magmatism and tectonics in the Alps. *Tectonics* 14, 120–131.
- Bonin, B., 2004. Do coeval mafic and felsic magmas in post-collisional to within-plate regimes necessarily imply two contrasting, mantle and crustal, sources? A review. *Lithos* 78, 1–24.
- Chemenda, A.I., Mattauer, M., Malavieille, J., Bokun, A.N., 1995. A mechanism for syn-collisional rock exhumation and associated normal faulting: results from physical modelling. *Earth and Planetary Science Letters* 132, 225–232.
- Chen, B., Jahn, B., Wei, C., 2002. Petrogenesis of Mesozoic granitoids in the Dabie UHP complex, Central China: trace element and Nd–Sr isotope evidence. *Lithos* 60, 67–88.
- Chen, D., Liu, L., Sun, Y., Liou, J., 2009. Geochemistry and zircon U–Pb dating and its implications of the Yukahe HP/UHP terrane, the North Qaidam, NW China. *Journal of Asian Earth Sciences* 35, 259–272.
- Chen, Y.X., Song, S.G., Niu, Y.L., Wei, C.J., 2014. Melting of continental crust during subduction initiation: a case study from the Chaidanuo peraluminous granite in the North Qilian suture zone. *Geochimica et Cosmochimica Acta* 132, 311–336.
- Chu, N.-C., Taylor, R.N., Chavagnac, V., Nesbitt, R.W., Boella, R.M., Milton, J.A., German, C.R., Bayon, G., Burton, K., 2002. Hf isotope ratio analysis using multi-collector inductively coupled plasma mass spectrometry: an evaluation of isobaric interference corrections. *Journal of Analytical Atomic Spectrometry* 17, 1567–1574.
- Chung, S.L., Chu, M.F., Zhang, Y., Xie, Y., Lo, C.H., Lee, T.Y., Lan, C.Y., Li, X., Zhang, Q., Wang, Y., 2005. Tibetan tectonic evolution inferred from spatial and temporal variations in post-collisional magmatism. *Earth-Science Reviews* 68, 173–196.
- Collins, W.J., 1994. Upper- and middle-crustal response to delamination: an example from the Lachlan fold belt, eastern Australia. *Geology* 22, 143–146.
- Collins, W., 1996. Lachlan Fold Belt granitoids: products of three-component mixing. *Transactions of the Royal Society of Edinburgh: Earth and Environmental Science* 87, 171–182.
- Coulon, C., Fourcade, S., Maury, R., Bellon, H., Louni-Hacini, A., Cotten, J., Coutelle, A., Hermitte, D., 2002. Post-collisional transition from calc-alkaline to alkaline volcanism during the Neogene in Oranie (Algeria): magmatic expression of a slab breakoff. *Lithos* 62, 87–110.
- Davies, J., von Blanckenburg, F., 1995. Slab breakoff: a model of lithosphere detachment and its test in the magmatism and deformation of collisional orogens. *Earth and Planetary Science Letters* 129, 85–102.
- Dewey, J., 1988. Extensional collapse of orogens. *Tectonics* 7, 1123–1139.
- Dias, G., Leterrier, J., Mendes, A., Simoes, P., Bertrand, J., 1998. U–Pb zircon and monazite geochronology of post-collisional Hercynian granitoids from the Central Iberian Zone (Northern Portugal). *Lithos* 45, 349–369.
- Douce, A.E.P., 1995. Experimental Generation of Hybrid Silicic Melts by Reaction of High-Al Basalt With Metamorphic Rocks.
- Douce, A.E.P., 1999. What do experiments tell us about the relative contributions of crust and mantle to the origin of granitic magmas? Geological Society, London, Special Publications 168, 55–75.
- Douce, A.E.P., Beard, J.S., 1995. Dehydration-melting of biotite gneiss and quartz amphibolite from 3 to 15 kbar. *Journal of Petrology* 36, 707–738.
- Douce, A.E.P., Johnston, A.D., 1991. Phase equilibria and melt productivity in the pelitic system: implications for the origin of peraluminous granitoids and aluminous granulites. *Contributions to Mineralogy and Petrology* 107, 202–218.
- Duggen, S., Hoernle, K., van den Bogaard, P., Garbe-Schönberg, D., 2005. Post-collisional transition from subduction- to intraplate-type magmatism in the westernmost Mediterranean: evidence for continental-edge delamination of subcontinental lithosphere. *Journal of Petrology* 46, 1155–1201.
- Falloon, T., Green, D., Hatton, C., Harris, K., 1988. Anhydrous partial melting of a fertile and depleted peridotite from 2 to 30 kbar and application to basalt petrogenesis. *Journal of Petrology* 29, 1257–1282.
- Faure, M., Bé Mézème, E., Cocherie, A., Rossi, P., Chemenda, A., Boutelier, D., 2008. Devonian geodynamic evolution of the Variscan Belt, insights from the French Massif Central and Massif Armoricain. *Tectonics* 27, TC2005.
- Faure, M., Cocherie, A., Bé Mézème, E., Charles, N., Rossi, P., 2010. Middle Carboniferous crustal melting in the Variscan Belt: new insights from U–Th–Pb zircon and U–Pb zircon ages of the Montagne Noire Axial Zone (southern French Massif Central). *Gondwana Research* 18, 653–673.
- Gehrels, G.E., Yin, A., Wang, X.-F., 2003. Magmatic history of the northeastern Tibetan Plateau. *Journal of Geophysical Research, Solid Earth* 108, 2423.
- He, Y., Li, S., Hoefs, J., Huang, F., Liu, S.-A., Hou, Z., 2011. Post-collisional granitoids of the Dabie orogen: new evidence for partial melting of a thickened continental crust. *Geochimica et Cosmochimica Acta* 75, 3815–3838.
- Hermann, J., Spandler, C.J., 2008. Sediment melts at sub-arc depths: an experimental study. *Journal of Petrology* 49, 717–740.
- Hibbard, M.J., 1991. Textural anatomy of twelve magma-mixed granitoid systems. In: Didier, J., Barbarin, B. (Eds.), *Enclaves and granite petrology*, Developments in Petrology 13. Elsevier, Amsterdam, pp. 431–444.
- Hirose, K., 1997. Melting experiments on herzolite KLB-1 under hydrous conditions and generation of high-magnesian andesitic melts. *Geology* 25, 42–44.
- Hirose, K., Kushiro, I., 1993. Partial melting of dry peridotites at high pressures: determination of compositions of melts segregated from peridotite using aggregates of diamond. *Earth and Planetary Science Letters* 114, 477–489.
- Hou, K., Li, Y., Zou, T., Qu, X., Shi, Y., Xie, G., 2007. Laser ablation-MC-ICP-MS technique for Hf isotope microanalysis of zircon and its geological applications. *Acta Petrologica Sinica* 23, 2595–2604.
- Houseman, G., McKenzie, D., Molnar, P., 1981. Convective instability of a thickened boundary layer and its relevance for the thermal evolution of continental convergent belts. *Journal of Geophysical Research* 86, 6115–6132.
- Huang, H., Niu, Y., Nowell, G., Zhao, Z., Yu, X., Zhu, D.-C., Mo, X., Ding, S., 2014. Geochemical constraints on the petrogenesis of granitoids in the East Kunlun Orogenic belt, northern Tibetan Plateau: implications for continental crust growth through syn-collisional felsic magmatism. *Chemical Geology* 370, 1–18.
- Jahn, B.-m., Wu, F.Y., Lo, C.-H., Tsai, C.-H., 1999. Crust–mantle interaction induced by deep subduction of the continental crust: geochemical and Sr–Nd isotopic evidence from post-collisional mafic–ultramafic intrusions of the northern Dabie complex, central China. *Chemical Geology* 157, 119–146.
- Jahn, B.-m., Cornichet, J., Cong, B., Yui, T.-F., 1996. Ultrahigh- $\epsilon$ Nd eclogites from an ultrahigh-pressure metamorphic terrane of China. *Chemical Geology* 127, 61–79.
- Jones, C.E., Tarney, J., Baker, J.H., Gerouki, F., 1992. Tertiary granitoids of Rhodope, northern Greece: magmatism related to extensional collapse of the Hellenic Orogen? *Tectonophysics* 210, 295–314.
- Kamei, A., Miyake, Y., Owada, M., Kimura, J.-I., 2009. A pseudo adakite derived from partial melting of tonalitic to granodioritic crust, Kyushu, southwest Japan arc. *Lithos* 112, 615–625.
- Kay, R.W., Mahlborg Kay, S., 1993. Delamination and delamination magmatism. *Tectonophysics* 219, 177–189.
- Kushiro, I., Syono, Y., Akimoto, S.-i., 1968. Melting of a peridotite nodule at high pressures and high water pressures. *Journal of Geophysical Research* 73, 6023–6029.
- Labrousse, L., Prouteau, G., Ganzhorn, A.-C., 2011. Continental exhumation triggered by partial melting at ultrahigh pressure. *Geology* 39, 1171–1174.
- Ledru, P., Courriou, G., Dallain, C., Lardeux, J., Montel, J., Vanderhaeghe, O., Vitel, G., 2001. The Velay dome (French Massif Central): melt generation and granite emplacement during orogenic evolution. *Tectonophysics* 342, 207–237.
- Li, S., Wang, C., Dong, F., Hou, Z., Li, Q., Liu, Y., Huang, F., Chen, F., 2009. Common Pb of UHP metamorphic rocks from the CCSZ project (100–5000 m) suggesting decoupling between the slices within subducting continental crust and multiple thin slab exhumation. *Tectonophysics* 475, 308–317.
- Liégeois, J.P., 1998. Some words on the post-collisional magmatism. *Lithos* 45, 15–18.
- Liégeois, J.P., Navez, J., Hertogen, J., Black, R., 1998. Contrasting origin of post-collisional high-K calc-alkaline and shoshonitic versus alkaline and peralkaline granitoids. The use of sliding normalization. *Lithos* 45, 1–28.
- Liu, Y., Li, S., 2008. Detachment within subducted continental crust and multi-slice successive exhumation of ultrahigh-pressure metamorphic rocks: evidence from the Dabie–Sulu orogenic belt. *Chinese Science Bulletin* 53, 3105–3119.
- Ludwig, K.R., 2003. *User's Manual for Isoplot 3.00: A Geochronological Toolkit for Microsoft Excel*. Kenneth R. Ludwig.
- Ma, C., Li, Z., Ehlers, C., Yang, K., 1998. A post-collisional magmatic plumbing system: Mesozoic granitoid plutons from the Dabieshan high-pressure and ultrahigh-pressure metamorphic zone, east-central China. *Lithos* 45, 431–456.
- Mattinson, C., Wooden, J., Liou, J., Bird, D., Wu, C., 2006a. Age and duration of eclogite-facies metamorphism, North Qaidam HP/UHP terrane, Western China. *American Journal of Science* 306, 683.
- Mattinson, C., Wooden, J., Liou, J., Bird, D., Wu, C., 2006b. Geochronology and tectonic significance of Middle Proterozoic granitic orthogneiss, North Qaidam HP/UHP terrane, Western China. *Mineralogy and Petrology* 88, 227–241.
- Mattinson, C.G., Menold, C.A., Zhang, J.X., Bird, D.K., 2007. High- and ultrahigh-pressure metamorphism in the North Qaidam and South Altyn Terranes, Western China. *International Geology Review* 49, 969–995.
- Mattinson, C., Wooden, J., Zhang, J., Bird, D., 2009. Paragneiss zircon geochronology and trace element geochemistry, North Qaidam HP/UHP terrane, western China. *Journal of Asian Earth Sciences* 35, 298–309.
- Meng, F., Zhang, J., 2008. Contemporaneous of Early Palaeozoic granite and high temperature metamorphism, North Qaidam Mountains, western Chin. *Acta Petrologica Sinica* 24, 1585–1594.
- Meng, F., Zhang, J., Yang, J., 2005. Tectono-thermal event of post-HP/UHP metamorphism in the Xitieshan area of the North Qaidam Mountains, western China: isotopic and geochemical evidence of granite and gneiss. *Acta Petrologica Sinica* 21, 45–56.
- Menold, C., Manning, C., Yin, A., Tropper, P., Chen, X.-H., Wang, X.-F., 2009. Metamorphic evolution, mineral chemistry and thermobarometry of orthogneiss hosting ultrahigh-pressure eclogites in the North Qaidam metamorphic belt, Western China. *Journal of Asian Earth Sciences* 35, 273–284.
- Miller, C.F., 1985. Are strongly peraluminous magmas derived from pelitic sedimentary sources? *The Journal of Geology* 673–689.
- Miller, C., Schuster, R., Klötzli, U., Frank, W., Purtscheller, F., 1999. Post-collisional potassic and ultrapotassic magmatism in SW Tibet: geochemical and Sr–Nd–Pb–O isotopic constraints for mantle source characteristics and petrogenesis. *Journal of Petrology* 40, 1399.
- Montel, J.-M., Vielzeuf, D., 1997. Partial melting of metagreywackes. Part II. Compositions of minerals and melts. *Contributions to Mineralogy and Petrology* 128, 176–196.
- Nelson, K., 1992. Are crustal thickness variations in old mountain belts like the Appalachians a consequence of lithospheric delamination? *Geology* 20, 498–502.
- Niu, Y., O'Hara, M.J., 2009. MORB mantle hosts the missing Eu (Sr, Nb, Ta and Ti) in the continental crust: new perspectives on crustal growth, crust–mantle differentiation and chemical structure of oceanic upper mantle. *Lithos* 112, 1–17.
- Niu, Y., Zhao, Z., Zhu, D.-C., Mo, X., 2013. Continental collision zones are primary sites for net continental crust growth—a testable hypothesis. *Earth-Science Reviews* 127, 96–110.
- O'Hara, M., 1965. Primary magmas and the origin of basalts. *Scottish Journal of Geology* 1, 19–40.
- Paquette, J.L., Ménot, R.P., Pin, C., Orsini, J.B., 2003. Episodic and short-lived granitic pulses in a post-collisional setting: evidence from precise U–Pb zircon dating through a crustal cross-section in Corsica. *Chemical Geology* 198, 1–20.
- Rapp, R.P., Watson, E.B., 1995. Dehydration melting of metabasalt at 8–32 kbar: implications for continental growth and crust–mantle recycling. *Journal of Petrology* 36, 891–931.
- Renna, M.R., Tribuzio, R., Tiepolo, M., 2006. Interaction between basic and acid magmas during the latest stages of the post-collisional Variscan evolution: clues from the gabbro-granite association of Ota (Corsica–Sardinia batholith). *Lithos* 90, 92–110.

- Rey, P., Vanderhaeghe, O., Teyssier, C., 2001. Gravitational collapse of the continental crust: definition, regimes and modes. *Tectonophysics* 342, 435–449.
- Roberts, M.P., Clemens, J.D., 1993. Origin of high-potassium, talc-alkaline, I-type granitoids. *Geology* 21, 825–828.
- Song, S.G., Yang, J.S., Liou, J.G., Wu, C.L., Shi, R.D., Xu, Z.Q., 2003a. Petrology, geochemistry and isotopic ages of eclogites from the Dulan UHPM Terrane, the North Qaidam, NW China. *Lithos* 70, 195–211.
- Song, S.G., Yang, J.S., Xu, Z.Q., Liou, J.G., Shi, R.D., 2003b. Metamorphic evolution of the coesite-bearing ultrahigh-pressure terrane in the North Qaidam, Northern Tibet, NW China. *Journal of Metamorphic Geology* 21, 631–644.
- Song, S.G., Zhang, L.F., Niu, Y.L., 2004. Ultra-deep origin of garnet peridotite from the North Qaidam ultrahigh-pressure belt, Northern Tibetan Plateau, NW China. *American Mineralogist* 89, 1330–1336.
- Song, S.G., Zhang, L.F., Niu, Y.L., Su, L., Jian, P., Liu, D.Y., 2005. Geochronology of diamond-bearing zircons from garnet peridotite in the North Qaidam UHPM belt, Northern Tibetan Plateau: a record of complex histories from oceanic lithosphere subduction to continental collision. *Earth and Planetary Science Letters* 234, 99–118.
- Song, S.G., Zhang, L.F., Niu, Y.L., Su, L., Song, B., Liu, D.Y., 2006. Evolution from oceanic subduction to continental collision: a case study from the northern Tibetan Plateau based on geochemical and geochronological data. *Journal of Petrology* 47, 435.
- Song, S.G., Su, L., Li, X.-h., Zhang, G.B., Niu, Y.L., Zhang, L.F., 2010. Tracing the 850-Ma continental flood basalts from a piece of subducted continental crust in the North Qaidam UHPM belt, NW China. *Precambrian Research* 183, 805–816.
- Song, S.G., Su, L., Li, X.H., Niu, Y.L., Zhang, L.F., 2012. Grenville-age orogenesis in the Qaidam–Qilian block: the link between South China and Tarim. *Precambrian Research* 220–221, 9–22.
- Song, S.G., Niu, Y.L., Su, L., Xia, X.H., 2013. Tectonics of the North Qilian orogen, NW China. *Gondwana Research* 23, 1378–1401.
- Song, S.G., Niu, Y.L., Su, L., Zhang, C., Zhang, L.F., 2014a. Continental orogenesis from ocean subduction, continent collision/subduction, to orogen collapse, and orogen recycling: the example of the North Qaidam UHPM belt, NW China. *Earth-Science Reviews* 129, 59–84.
- Song, S.G., Niu, Y.L., Su, L., Wei, C.J., Zhang, L.F., 2014b. Adakitic (tonalitic–trondhjemitic) magmas resulting from eclogite decompression and dehydration melting during exhumation in response to continental collision. *Geochimica et Cosmochimica Acta* 130, 42–62.
- Sun, S.S., McDonough, W.F., 1989. Chemical and isotopic systematics of oceanic basalts: implications for mantle composition and processes. Geological Society, London, Special Publications 42, 313–345.
- Sylvester, P.J., 1998. Post-collisional strongly peraluminous granites. *Lithos* 45, 29–44.
- Turner, S., Arnaud, N., Liu, J., Rogers, N., Hawkesworth, C., Harris, N., Kelley, S., Van Calsteren, P., Deng, W., 1996. Post-collision, shoshonitic volcanism on the Tibetan Plateau: implications for convective thinning of the lithosphere and the source of ocean island basalts. *Journal of Petrology* 37, 45.
- Turner, S., Platt, J., George, R., Kelley, S., Pearson, D., Nowell, G., 1999. Magmatism associated with orogenic collapse of the Betic–Alboran domain, SE Spain. *Journal of Petrology* 40, 1011–1036.
- Vielzeuf, D., Montel, J.M., 1994. Partial melting of metagreywackes. Part I. Fluid-absent experiments and phase relationships. *Contributions to Mineralogy and Petrology* 117, 375–393.
- Wallis, S., Tsuboi, M., Suzuki, K., Fanning, M., Jiang, L., Tanaka, T., 2005. Role of partial melting in the evolution of the Sulu (eastern China) ultrahigh-pressure terrane. *Geology* 33, 129–132.
- Wan, Y., Xu, Z., Yang, J., Zhang, J., 2001. Ages and compositions of the Precambrian high-grade basement of the Qilian terrane and its adjacent areas. *Acta Geologica Sinica-English Edition* 75, 375–384.
- Wan, Y., Zhang, J., Yang, J., Xu, Z., 2006. Geochemistry of high-grade metamorphic rocks of the North Qaidam mountains and their geological significance. *Journal of Asian Earth Sciences* 28, 174–184.
- Warren, C.J., Beaumont, C., Jamieson, R.A., 2008. Formation and exhumation of ultra-high-pressure rocks during continental collision: role of detachment in the subduction channel. *Geochemistry, Geophysics, Geosystems* 9.
- Whalen, J.B., McNicoll, V.J., van Staal, C.R., Lissenberg, C.J., Longstaffe, F.J., Jenner, G.A., van Breeman, O., 2006. Spatial, temporal and geochemical characteristics of Silurian collision-zone magmatism, Newfoundland Appalachians: an example of a rapidly evolving magmatic system related to slab break-off. *Lithos* 89, 377–404.
- Whitney, D.L., Teyssier, C., Fayon, A.K., 2004. Isothermal decompression, partial melting and exhumation of deep continental crust. Geological Society, London, Special Publications 227, 313–326.
- Williams, H., Turner, S., Kelley, S., Harris, N., 2001. Age and composition of dikes in Southern Tibet: new constraints on the timing of east–west extension and its relationship to postcollisional volcanism. *Geology* 29, 339.
- Wu, F.-Y., Jahn, B.-m., Wilde, S., Sun, D.-y., 2000. Phanerozoic crustal growth: U–Pb and Sr–Nd isotopic evidence from the granites in northeastern China. *Tectonophysics* 328, 89–113.
- Wu, C., Wooden, J.L., Yang, J., Robinson, P.T., Zheng, L., Shi, R., Chen, S., 2006a. Granitic magmatism in the North Qaidam Early Paleozoic ultrahigh-pressure metamorphic belt, northwest China. *International Geology Review* 48, 223–240.
- Wu, F.-Y., Yang, Y.-H., Xie, L.-W., Yang, J.-H., Xu, P., 2006b. Hf isotopic compositions of the standard zircons and baddeleyites used in U–Pb geochronology. *Chemical Geology* 234, 105–126.
- Wu, C., Gao, Y., Wu, S., Chen, Q., Wooden, J., Mazadab, F., Mattinson, C., 2007. Zircon SHRIMP U–Pb dating of granites from the Da Qaidam area in the north margin of Qaidam Basin, NW China. *Acta Petrologica Sinica* 23, 1861–1875 (in Chinese with English abstract).
- Wu, C., Wooden, J.L., Robinson, P.T., Gao, Y., Wu, S., Chen, Q., Mazdab, F.K., Mattinson, C., 2009. Geochemistry and zircon SHRIMP U–Pb dating of granitoids from the west segment of the North Qaidam. *Science in China Series D: Earth Sciences* 52, 1771–1790.
- Xu, J.-F., Shinjo, R., Defant, M.J., Wang, Q., Rapp, R.P., 2002. Origin of Mesozoic adakitic intrusive rocks in the Ningzhen area of east China: partial melting of delaminated lower continental crust? *Geology* 30, 1111–1114.
- Xu, H., Ma, C., Ye, K., 2007. Early cretaceous granitoids and their implications for the collapse of the Dabie orogen, eastern China: SHRIMP zircon U–Pb dating and geochemistry. *Chemical Geology* 240, 238–259.
- Yamato, P., Burov, E., Agard, P., Le Pourhiet, L., Jolivet, L., 2008. HP–UHP exhumation during slow continental subduction: self-consistent thermodynamically and thermomechanically coupled model with application to the Western Alps. *Earth and Planetary Science Letters* 271, 63–74.
- Yang, J., Xu, Z., Zhang, J., Song, S., Wu, C., Shi, R., Li, H., Brunel, M., 2002a. Early Palaeozoic North Qaidam UHP metamorphic belt on the north-eastern Tibetan plateau and a paired subduction model. *Terra Nova* 14, 397–404.
- Yang, J., Xu, Z., Zhang, J., Song, S., Wu, C., Shi, R., Li, H., Brunel, M., 2002b. Two contrasting magmatic events in the Dulan UHP metamorphic terrane; Implication for collisional orogeny. *Acta Petrologica Sinica* 27, 3335–3349.
- Yang, J., Wu, F., Chung, S.-L., Wilde, S.A., Chu, M., Lo, C., Song, B., 2005. Petrogenesis of Early Cretaceous intrusions in the Sulu ultrahigh-pressure orogenic belt, east China and their relationship to lithospheric thinning. *Chemical Geology* 222, 200–231.
- Yang, J., Wu, F., Wilde, S.A., Liu, X., 2007. Petrogenesis of Late Triassic granitoids and their enclaves with implications for post-collisional lithospheric thinning of the Liaodong Peninsula, North China Craton. *Chemical Geology* 242, 155–175.
- Yu, S., Zhang, J., Del Real, P.G., 2012. Geochemistry and zircon U–Pb ages of adakitic rocks from the Dulan area of the North Qaidam UHP terrane, north Tibet: Constraints on the timing and nature of regional tectonothermal events associated with collisional orogeny. *Gondwana Research* 21, 167–179.
- Zhang, J., Yang, J., Mattinson, C., Xu, Z., Meng, F., Shi, R., 2005. Two contrasting eclogite cooling histories, North Qaidam HP/UHP terrane, western China: petrological and isotopic constraints. *Lithos* 84, 51–76.
- Zhang, J., Yang, J., Meng, F., Wan, Y., Li, H., Wu, C., 2006. U–Pb isotopic studies of eclogites and their host gneisses in the Xitieshan area of the North Qaidam mountains, western China: new evidence for an early Paleozoic HP–UHP metamorphic belt. *Journal of Asian Earth Sciences* 28, 143–150.
- Zhang, G., Song, S., Zhang, L., Niu, Y., 2008a. The subducted oceanic crust within continental-type UHP metamorphic belt in the North Qaidam, NW China: evidence from petrology, geochemistry and geochronology. *Lithos* 104, 99–118.
- Zhang, J., Mattinson, C.G., Meng, F., Wan, Y., Tung, K., 2008b. Polyphase tectonothermal history recorded in granulitized gneisses from the north Qaidam HP/UHP metamorphic terrane, western China: evidence from zircon U–Pb geochronology. *Geological Society of America Bulletin* 120, 732–749.
- Zhang, G., Ellis, D.J., Christy, A.G., Zhang, L., Niu, Y., Song, S., 2009. UHP metamorphic evolution of coesite-bearing eclogite from the Yuka terrane, North Qaidam UHPM belt, NW China. *European Journal of Mineralogy* 21, 1287–1300.
- Zhang, J., Mattinson, C., Yu, S., Li, J., Meng, F., 2010. U–Pb zircon geochronology of coesite-bearing eclogites from the southern Dulan area of the North Qaidam UHP terrane, northwestern China: spatially and temporally extensive UHP metamorphism during continental subduction. *Journal of Metamorphic Geology* 28, 955–978.
- Zhao, Z.-F., Zheng, Y.F., Wei, C.S., Wu, Y.B., 2007. Post-collisional granitoids from the Dabie orogen in China: zircon U–Pb age, element and O isotope evidence for recycling of subducted continental crust. *Lithos* 93, 248–272.
- Zhao, Z.-F., Zheng, Y.-F., Wei, C.-S., Wu, F.-Y., 2011. Origin of postcollisional magmatic rocks in the Dabie orogen: implications for crust–mantle interaction and crustal architecture. *Lithos* 126, 99–114.
- Zhao, Z.-F., Zheng, Y.-F., Zhang, J., Dai, L.-Q., Li, Q., Liu, X., 2012. Syn-exhumation magmatism during continental collision: evidence from alkaline intrusives of Triassic age in the Sulu orogen. *Chemical Geology* 328, 70–88.
- Zheng, Y.-F., Xia, Q.-X., Chen, R.-X., Gao, X.-Y., 2011. Partial melting, fluid supercriticality and element mobility in ultrahigh-pressure metamorphic rocks during continental collision. *Earth-Science Reviews* 107, 342–374.